Minimizing Aerodynamic Disturbances and Particle Release Risk of Fibrous Filters of a Novel Air Purification System

by

Erfan Rasouli

A thesis submitted in partial fulfillment of the requirements for the degree of

Master of Science

Department of Mechanical Engineering
University of Alberta

Abstract

This study investigates the aerodynamic performance of a novel heat-based air disinfection system equipped with pleated fibrous filters. A key feature of the system is the presence of mechanical gates located upstream and downstream of the disinfection units. These gates are essential parts of the system, as they regulate airflow and isolate the units during the disinfection process. However, their movement can generate aerodynamic disturbances, which may lead to the release of particles entrapped within the filters. Thus, numerical and experimental tests were employed to investigate how gates and their movement affect the airflow.

The number of gates and the rotation period during their opening and closing substantially affect the flow pattern. Thus, configurations with 1 to 4 gates on each side of the units, along with three gate movement durations, were tested. The goal was to find the best arrangement that results in the least flow agitation.

Numerical simulations were conducted to analyze the transient flow characteristics. It is known that high flow acceleration, velocity, and turbulent kinetic energy (TKE) can increase aerodynamic forces on particles within the filters and therefore release particles from them. Thus, they were monitored and minimized on the filter surface by testing the different gate configurations and rotation periods.

The results demonstrate that the unit with 4-gates has the least aerodynamic disturbances, and it consistently yields considerably lower TKE, maximum velocity, and acceleration compared to the other setups. Additionally, longer gate movement periods significantly reduced flow acceleration and turbulence growth, which further reduces the particle release risk.

Experimental tests also confirmed that rapid gate movement triggers particle emissions from loaded filters. A 10-time rapid gate movement led to about 5% re-entrainment of the particles within the filter, and reducing the gate movement period yielded 10 times lower particle release. Overall, the results provide practical insights for the design and operation of the disinfection system with minimal hazardous particle release risk.

Preface

This research is the original work by Erfan Rasouli. The experiments, their design, and equipment calibration were mainly done in collaboration with Dr. Mahmood Salimi. Additionally, the wind tunnel setup was originally designed by Ali Mirzazadeh Akbarpoor and Dr. Mahmood Salimi and constructed in collaboration with Dr. Mahmood Salimi, Adib Shabani, and Sam Sarkar. No part of this research has been previously published.

Acknowledgement

I extend my deepest gratitude to my research supervisors, Dr. Alireza Nouri and Dr. Mahdi Shahbakhit, as well as Dr. Mahmood Salimi, the lab research assistant, for their unwavering support, guidance, and insightful feedback throughout this project. Their critical input and encouragement were essential to the completion of this work.

I am also grateful to my lab mates and friends, Ali Mirzazadeh, Adib Shabani, and Matin Moghtader, for their consistent assistance, collaboration, and support during my program.

This research was made possible through the generous funding and support of the Natural Sciences and Engineering Research Council of Canada (NSERC) and Engineered Air, whose contributions made experimental work and equipment procurement possible. I sincerely appreciate their support and the resources they provided for our research team.

Finally, I would like to express my heartfelt thanks to my family for their constant encouragement, patience, and emotional support throughout my academic journey. Their belief in me has been a source of strength and motivation.

Table of Contents

List of Tables

List of Figures

Nomenclature

Symbol	Definition	Symbol	Definition
C_i	Inertial resistance (1/m)	P_k	Production rate of turbulent kinetic energy ($kg/m^3.s^2$)
C_μ	Empirical model constant	P_ω	Production rate of specific dissipation rate ($kg/m^3.s^2$)
CFM	Cubic feet per meter (ft^3)	Q	Volumetric flow rate (m^3/s)
d	Diameter (m)	Re	Reynolds number
dP	Pressure drop (Pa)	S	Source term
F	Force (N)	t	Time (s)
F1	Blending function	TKE	Turbulent kinetic energy (m^2/s^2)
k	Turbulent kinetic energy (m^2/s^2)	V	Velocity (m/s)
L	Gate Length (m)	V'	Fluctuating velocity (m/s)
L'	Channel height (m)	x	Spatial coordinate (m)
n	Porous media thickness (m)	y	Spatial coordinate (m)
P	Pressure (Pa)	h	Hour
m	meter		
Greek		**Subscript**	
ϑ	Particle volume (m^3)	PG	Pressure Gradient
ρ	Density (kg/m^3)	p	Particle
α	Permeability (m^2)	f	Fluid
β	Equation constant	i	index
β^*	Empirical model constant	j	index
μ	Dynamic viscosity (Pa.s)	t	turbulent
ω	Specific dissipation rate (1/s)	ave	Average
γ	Empirical model constant		
σ_k	Empirical model constant	**Superscript**	
σ_ω	Empirical model constant	n	Time step
λ	Equation constant		
ϵ	Dissipation rate (m^2/s^3)		
ν	Kinematic viscosity (m^2/s)		
π	Pi number		

Chapter 1- Introduction & Background

1-1- Preface

In the modern era, people spend a significant portion of their daily lives indoors, primarily due to prevailing lifestyles and work environments. Regardless of a building's specific purpose, heating, ventilation, and air conditioning (HVAC) systems are integral to its overall design. These systems are essential for providing a continuous supply of fresh and purified air to occupants using thermal processes and air circulation using both outdoor and indoor sources.

While HVAC systems are crucial in maintaining indoor air quality, they can also pose a potential risk by facilitating the transmission of infectious pathogens to various sections of a building and endangering the health of its occupants. Considering that pathogens can become airborne and travel in the form of aerosols, air conditioning systems and ductwork, which are responsible for air recirculation within buildings, can serve as conduits for these pathogens to spread throughout the building and risk the well-being of individuals [1].

Consequently, it becomes imperative to equip air conditioning systems with air purification systems that are efficient, cost-effective, and easy to install. To address this concern, scientists have developed a range of technologies, a focus that has intensified significantly following the COVID-19 pandemic.

1-2-Overview and Problem Statement

This thesis aims to benefit from thermal disinfection by combining it with filtration technology. The proposed novel and innovative approach will be able to disinfect the air at a reasonably low temperature and provide continuous, clean airflow.

Figure 1-1 illustrates the schematic of the disinfection system and its operation modes investigated in this thesis. As can be seen, it mainly consists of two side-by-side units, two air filters, two heating elements in front of each filter, and gates in the front and rear sections of the units.

The disinfection units have three operation modes. In the first mode, one of the units is closed and the other one remains open. The heater of the closed unit starts to heat the filter and pathogens entrapped in it. Meanwhile, the other unit’s gates are open, and it continues to capture harmful particles and provide continuous and pathogen-free airflow. When full disinfection is achieved, the

gates of the closed unit are opened. In the second mode, the same process is repeated for the second unit. The first unit is kept open, the second unit is closed, and thermal disinfection is applied in the second unit. In the third mode, the gates of both units are open, and the air flows through both filters, and the filters capture particles and pathogens in the air.

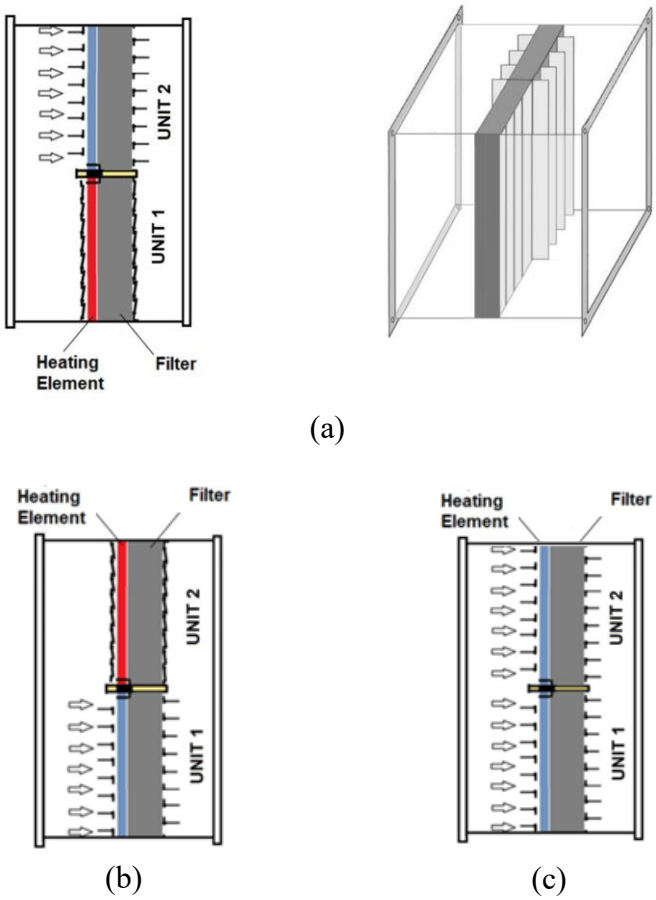

Figure 1-1- Schematic and operation modes of the disinfection units built in Filtration Testing Lab: a) Mode 1, b) Mode 2, c) Mode 3

The primary idea behind this configuration is the need for disinfecting the filters and reducing the energy consumption required for the process. Filters constantly purify the air by capturing particles in it. Yet, these particles can be hazardous pathogens, and they are not inactivated and can still create health hazards for the person who changes the filters. In addition, any disturbance to airflow may cause some of the entrapped particles to be released into the environment. Thus, it is crucial to disinfect them.

Furthermore, it will be seen in the literature review part, the temperature requirement for disinfecting the rapid single pass airflow is significant. In contrast, in an isolated medium, much

lower temperatures can be used for effective disinfection, but the time required for disinfection is relatively long. By isolating one of the units while the other one is open, two goals are achieved. Firstly, when the unit is closed, there is no airflow in it. Thus, the disinfection time can be prolonged, meaning that low temperatures can be used to inactivate pathogens. Secondly, one of the units is always open, and it continuously provides clean air to building occupants.

The main concern of this thesis is related to the gate movement. The system requires an isolated medium for the disinfection process. Thus, the gates should shut off the airflow so that the heater can inactivate pathogens entrapped within the filter. However, during the opening and closing movements of the gates, the flow can be agitated, and strong velocity fluctuations can occur. This flow agitation can disturb the filter loaded with particles and re-entrain particles into the airflow downstream of the units.

1-3- Research Objectives

The disinfection unit gates are obstacles in front of the air entering the unit, and their presence and rotation disturb the flow. Accordingly, this research aims to study the effects of the gates' rotation on the airflow inside the disinfection units and minimize the flow disturbance caused by them.

Since the flow and filter agitation are unfavorable, this thesis focuses on minimizing the flow agitation and filter disturbance inside the disinfection units. This will be achieved by studying the effects of the gates' rotation speed as well as the number of gates located upstream and downstream of the disinfection units.

1-4- Research Hypothesis

The following hypotheses are proposed for investigating the effects of moving gates on the flow characteristics and particle release:

1- The movement of the gates can induce flow disturbances, create vortices, and increase turbulence inside the unit.
2- The movement of the gates can also affect airflow velocity, acceleration, and pressure on the filter surface, thereby increasing the aerodynamic forces on the filter and entrapped particles.
3- Increasing aerodynamic tensions on the filter inside the unit can dislodge particles entrapped in it.

4- Increasing the number of gates on the front and rear sides of the disinfection units may lead to a more uniform flow with lower flow disturbance inside the units as compared to the units with a lower number of gates.
5- The gate movement speed can significantly affect the flow, and sudden gate movements can lead to large transient flow changes. This can increase particle release from the filters.

The figure below displays an exaggerated version of the hypothesis of this research. The gates can disturb the flow and create vortices upstream of the filter. This flow disturbance can lead to particle release from the filter.

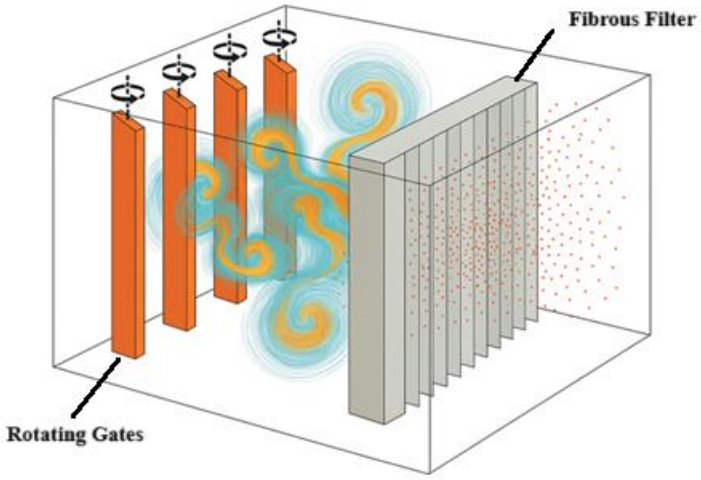

Figure 1-2- Flow disturbance due to gate movement and particle release from the filter

1-5- Research Methodology

Numerical and experimental tests will be designed and employed to investigate the hypotheses of this thesis. Accurately measuring and visualizing the velocity distribution and transient changes with experiments is difficult, costly, and time-consuming. On the other hand, performing numerical simulations does not require any experimental setup, and they can provide an excellent representation of the flow patterns and velocity distribution. Thus, simulations will be used to study how gate rotation influences the flow pattern inside the disinfection unit.

The system will be simulated using the Ansys Fluent 2023 R2 software. For conducting numerical research, first, the numerical model will be created. Then, the model will be validated against experimental data. After ensuring the validity of the model, the objectives of this research will be explored.

Furthermore, simulations fall short in modeling particle movement inside a filter medium under turbulent flow. Therefore, experiments will be done to support the hypothesis that gate movement can intensify airflow disturbance and detach particles from the filters.

Figure 1-3 illustrates the overall methodology of this thesis. The literature review part will cover the existing commonly used air purification technologies to check the viability of the technology used in this project. The key parameters affecting the particle release and the numerical methods for simulating HVAC filters will also be explored.

After reviewing the literature, the research gap, key parameters affecting particle release, and a suitable numerical model will be identified.

Then, the numerical model will be developed, and different disinfection unit configurations with various numbers of gates and rotation speeds will be simulated. Experiments will also be used to verify that increasing aerodynamic disturbances and tensions on the filter will increase the particle release from the loaded filters.

Finally, the outcomes of the numerical tests will be investigated to identify the best configuration having the least amount of flow disturbance and particle release risk.

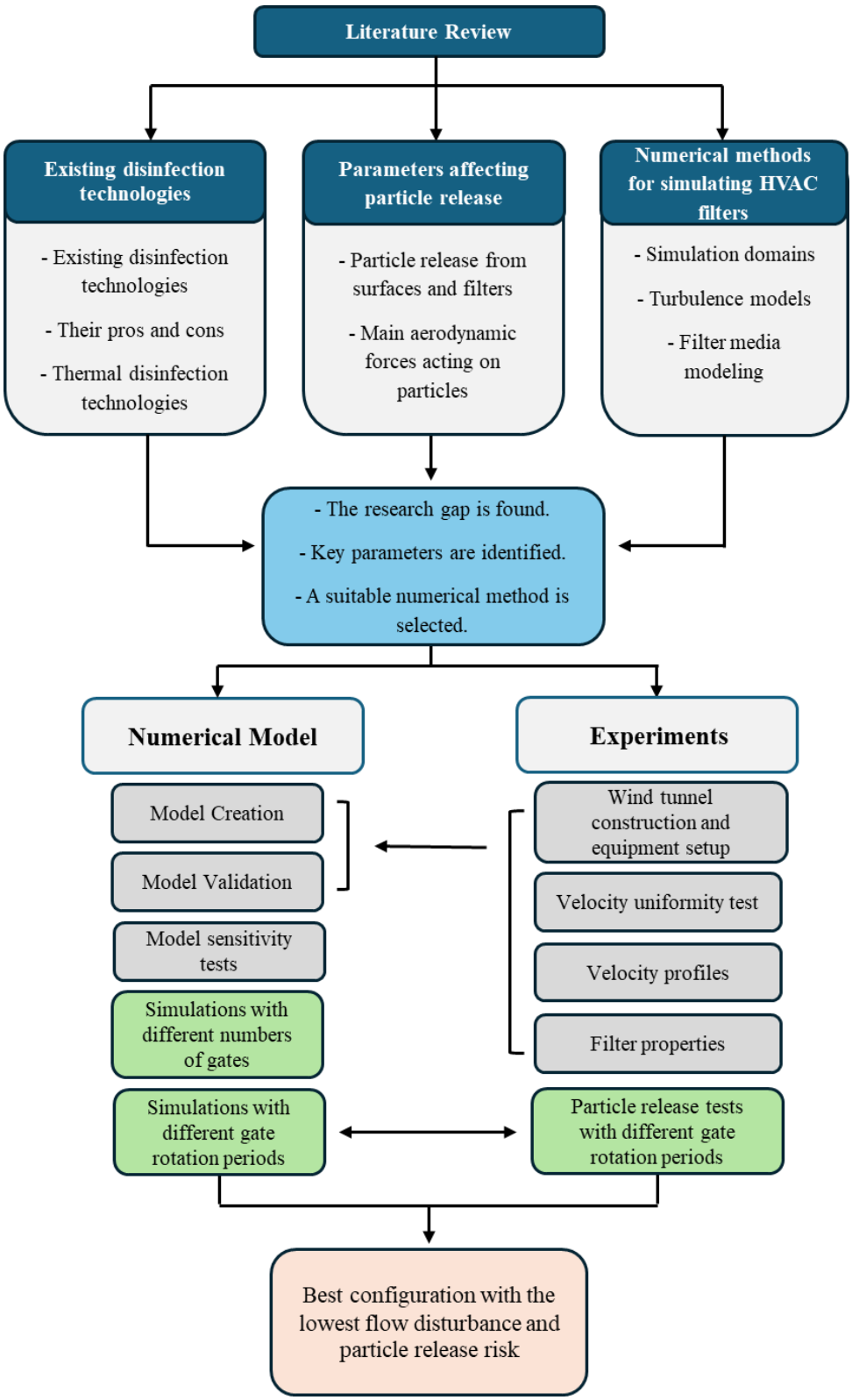

Figure 1-3- Overall research methodology – The gray boxes under the Experiments and Numerical Model boxes are required for developing the numerical model. The green boxes indicate the main steps for finding the best configuration of gates

1-6- Thesis Outline

This thesis includes 6 main chapters. The content of each chapter is briefly introduced below.

Chapter 1 introduces the air disinfection system, its operating mechanism, and the main concerns associated with it. It also presents the research objectives, the developed hypothesis, and the methodology employed for conducting this research.

Chapter 2 is a comprehensive research review, and it explores the existing technologies, particle detachment from various surfaces and filters, and relevant numerical methodologies. Then, the research gap, key parameters involved in particle disturbance, and a suitable numerical method are identified. These parameters are used as the objective parameters in the simulations.

Chapter 3 outlines the overall methodological approach, which includes both numerical and experimental components of this study. It explains the experiments, equipment, and methods used for obtaining the data required in numerical simulations.

Chapter 4 provides detailed information about the numerical model development and simulation setups with various configurations.

Chapter 5 discusses the results, and it presents and analyzes the results of the numerical and experimental tests. This chapter includes the effects of the number of gates and the gate rotation periods on the flow pattern and particle release. It also compares the numerical and experimental findings. Finally, various configurations with different gate numbers and gate rotation periods are evaluated to find the optimal configuration with the least amount of flow disturbance and particle release risk.

Chapter 6, the conclusion chapter, summarizes the key findings of this research. Additionally, it discusses the limitations faced during this research and provides recommendations for future research work.

The thesis ends with references and appendices. The references cited in this research and supplementary data are included in this section.

Chapter 2- Literature Review & Research Gap

2-1- Preface

This chapter studies various commonly used disinfection technologies, their pros and cons, and technologies that have investigated pathogen inactivation specifically with thermal disinfection. In addition, the studies related to particle release from various surfaces, including HVAC filters and flat surfaces, and important parameters affecting particle release are discussed. Finally, the numerical research and methods for simulating flow through HVAC filters are explained and summarized.

2-2- Existing Commonly Used Technologies for Pathogen Protection

Over the past few decades, various technologies have been developed to protect indoor environments against pathogens. The most common technologies used in buildings include filtration, electrostatic filters, biocidal coatings, ultraviolet irradiation, and so forth. These technologies will be briefly discussed in the following sections.

2-2-1- Filtration

One of the most prevalent techniques employed in HVAC systems is the use of fibrous filters to separate particles from air. These readily available filters consist of very fine fibrous pores. As air passes through these filters, the fibrous porous media capture the particles with diameters less than the filter's pores [2]. This way, filters purify the air passing through them. Additionally, these filters are commonly designed in a pleated configuration, which serves to increase the filtration surface area and enhance particle entrapment efficiency [3]. Moreover, supportive strips are usually added to the filter frame to increase its mechanical strength against relatively high air velocities. An illustrative example of such filters can be observed in Figure 2-1 [3].

Among the various air filtration solutions proposed by scientists, the most effective option is the high-efficiency particulate absorbing (HEPA) filters which can capture 99.9% of the particles and pathogens with diameters more than 0.3 micrometers in the air [4]. While these filters offer exceptional efficiency, their relatively high cost and the excessive pressure drop have limited their widespread adoption in residential settings. Thus, they are mostly used in large facilities with high air quality standards, such as hospitals and clean rooms [5].

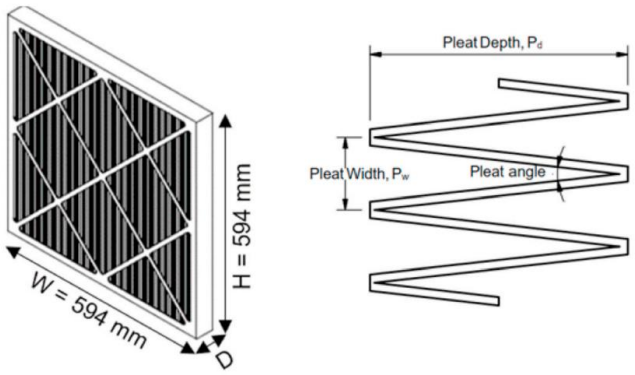

Figure 2-1- Schematic of an HVAC pleated filter [3]

In response to this, manufacturers have developed filters with larger pore diameters, which prove to be effective in capturing larger airborne particles like dust. These filters are categorized based on their efficiency using the Minimum Efficiency Reporting Value (MERV) system, with HEPA filters surpassing the MERV 16 grade. Additionally, the American Society of Heating, Refrigeration, and Air Conditioning (ASHRAE) suggests using MERV 13 filters where possible in buildings to promote indoor air quality [6].

2-2-2- Electrostatic Filtration and Biocidal Filters

Although filters primarily capture particles, pathogens remain active even when they are trapped within them. Thus, scientists have suggested strategies to promote conventional filters. One approach is to use electrostatic filters. By reinforcing filters with electrostatic forces, manufacturers add Coulombic attraction and electrophoresis particle-capturing mechanisms to filters, which leads to higher efficiency and lower pressure drop [7]. Another effective approach is adding a biocidal function to filters by incorporating antimicrobial or antiviral materials into them. These materials include metallic nanoparticles such as Ag and ZnO. In this way, the entrapped pathogens are inactivated as well and cannot continue to grow or colonize on filter surfaces [8].

2-2-3- Ultraviolet Irradiation

Utilizing ultraviolet (UV) radiation in HVAC systems is one of the most common disinfection technologies. By incorporating UV lamps inside an HVAC system or duct, engineers use UV radiation to kill and inactivate pathogens. It is proven that the UV radiation can denature a broad range of pathogens, including SARS-CoV-2, MS2, and various bacteria [9–12]. While using the same disinfection principle, the UV lamps can be mercury-based and mercury-free, based on the

application, and it is proven that the mercury-free lamps can outperform the conventional mercury-based UV lamps [13].

2-2-4- Ozonation and Plasma Disinfection

In addition to UV technology, some scientists have developed alternative approaches to disinfect air, one of which is ozonation. Ozone is a highly effective oxidant, which is capable of disinfecting air by easily oxidizing a wide range of microorganisms or harmful particles in it. Thus, it can be used to inactivate pathogens [14]. Thus, using plasma for disinfecting air has gained attention in recent years. Nonthermal plasma can be used to generate reactive species such as reactive oxygen species, reactive nitrogen species, and UV photons. By exposing air to these reactive species, air sterilization can be achieved [15].

2-2-5- Photocatalysis and Microwave Inactivation

Photocatalysis and microwave disinfection are two other technologies scientists use to inactivate pathogens. In the photocatalysis method, photocatalysts such as TiO2 are applied to a surface. When a light source (commonly UV) irradiates these photocatalysts, they create electron-hole pairs which produce reactive species and free radicals with a short lifetime. Then, these species oxide and inactivate pathogens, and it is shown that this method can be 90% effective in removing hazardous particles in the air [16]. In the microwave approach, air is heated by using microwave irradiation. The electromagnetic waves produced by microwave devices can interact with air, water, or other polar molecules and increase their temperature, and through this temperature rise and radiation effects, microwave technology can denature and inactivate pathogens [17].

2-2-6- Thermal Inactivation

As mentioned in the microwave technology section, high temperatures can affect pathogens and inactivate them. The primary mechanism used in thermal disinfection is breaking down the constituent parts of pathogens using high temperatures and heat, which leads to inactivation and infectious ability loss of the pathogens. Thus, scientists have proposed thermal disinfection as an alternative disinfection approach that can provide 99.9% efficiency in inactivating pathogens.

According to Vlaskin and Bertrand et al [18-19], temperatures higher than 50°C can denature pathogens including SARS-CoV-2 and successfully inactivate them with 99.9% efficiency without

generating any hazardous by-products or harmful radiations. Additionally, heating a medium can be done by using a simple electric heater, which is practical and easy to use.

However, the time required for the inactivation at lower temperatures is considerable. Thus, temperature and time are the most important factors in thermal deactivation, and unlike UV disinfection, thermal inactivation has very low dependence on humidity levels of air [20-21]. For rapid, single-pass disinfection, higher temperatures are therefore necessary.

The following sections review the required temperature and exposure durations for effective pathogen inactivation in both flowing and stationary air systems.

2-2-6-1- Thermal Disinfection of Flowing Air

When it comes to disinfecting the flowing air in a single-pass manner, the available time for heating the air and increasing its temperature can be very short, depending on the flow rate. This necessitates the application of high temperatures to make sure all pathogens experience a major temperature increase and are inactivated. For example, Grinshpun et al. [22] studied the inactivation of the aerosolized MS2 virus. They used axial heating to disinfect air with 18 l/min and 36 l/min flow rates, and they considered 0.1~1s exposure time for heating the air. After conducting tests, they concluded that increasing the temperature to 90°C (Q=18 l/min) and 140°C (Q=36 l/min) will result in moderate infectivity reduction. To maximize the inactivation and reach 99.996% disinfection, they illustrated that they needed to significantly raise the temperatures to 170°C (Q=18 l/min) and 250°C (Q=36 l/min).

Canpolat et al. [23] utilized thermal heating to inactivate the SARS-CoV-2 virus in air with a 10 l/min flow rate in a prototype with a 4 cm by 4cm cross-section (Figure 2-2). They passed the contaminated air through a wind tunnel equipped with electrical heater coils and exposed the air to high heat for 1.44s. Their experiments indicated that 99.9% and 99.999% inactivation efficiencies are attainable when the air exit temperatures are 150°C and 220°C, respectively.

In an interesting approach, Yu et al. [24] combined filtration and thermal heating technologies to inactivate the SARS-CoV-2 virus and Bacillus anthracis spore in air with a 10 l/min flow rate. They used a filter made of nickel foam with very fine pores, and they also turned this metallic foam into an electric heater by connecting it to electricity. In this way, the porous media entrapped the virus particles, and the heat inactivated them. The results of this paper illustrated that this technology

could inactivate 99.9% of SARS-CoV-2 viruses and 99.99% of Bacillus anthracis spores in a single pass when the filter temperature is increased up to 200°C.

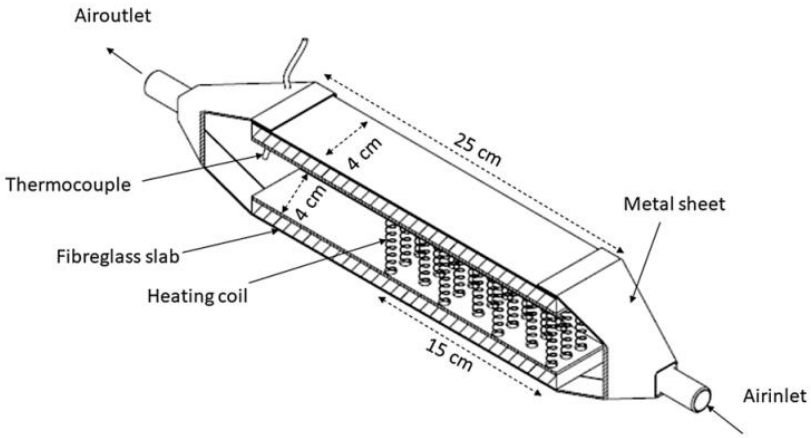

Figure 2-2- Schematic of the wind tunnel used in Canpolat's study [23]

In a similar approach, Zarghanishiraz et al. [25] configured finely woven nichrome heating wires in a porous shape with consecutive layers (Figure 2-3) to inactivate the SARS-CoV-2 virus and numerically studied the particle capturing efficiency of this filter by using the Lagrangian particle tracking approach. The airflow rate was 5000 l/min, and they increased the heating wires' temperature to 150°C to achieve complete virus inactivation. They researched the effect of particle diameter as well as the distance between filtering layers on the filtration efficiency, and their simulations indicated that their woven wire filter configuration is highly efficient for capturing particles with 3 μm diameter. However, this efficiency fell below 50% for particles with diameters less than 1 μm.

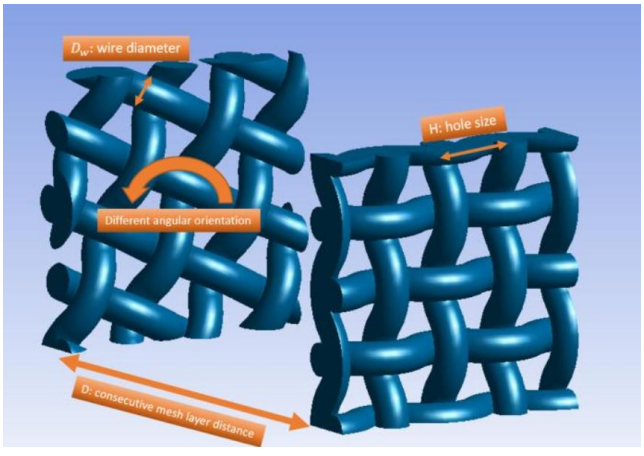

Figure 2-3- The woven heating wires in Zarghanishiraz's study [25]

2-2-6-2- Thermal Disinfection of Stationary Air

In contrast to single-pass thermal disinfection, inactivating pathogens in stationary air or inside a container has much less strict time and temperature requirements. According to Zou et al. [26], completely inactivating avian influenza H7N9 virus is possible by heating a medium for 30 minutes at 56°C, 10 minutes at 65°C, and 1 minute at 100°C. Additionally, Hessling et al. [27] reported that the influenza virus loses its infectivity on various surfaces when they are heated for less than 10 minutes at 65°C. Johne et al. [28] studied the thermal stability of the Hepatitis E virus by using the cell culture method, and reported that a 2log10 infectivity reduction is possible by exposing the virus to 65°C for 1 minute. Leclercq et al. [29] investigated the stability of the MERS-CoV virus against heat. Their results indicated that 56°C with a 25-minute duration and 65°C with a 15-minute duration will eliminate the infection risk of this virus.

The thermal inactivation of different species of the COVID-19 virus is also possible with temperatures below 70°C. For example, Batejat et al. [30] exposed different samples spiked with the SARS-CoV-2 virus to high temperatures and concluded that the virus can be inactivated in less than 30, 15, and 3 minutes if it is heated at 56, 65, and 95°C temperatures, respectively. In a valuable effort, Yap et al. [31] did a thermodynamic analysis on existing data for thermal inactivation of SARS-CoV-1, SARS-CoV-2, and SARS-CoV-3, and developed a model for predicting the required time for different temperatures to decontaminate these viruses. Accordingly, they reported that using 60°C for 10.5 minutes can yield 3log10 (99.9%) decontamination for SARS-CoV-2.

Table 2-1 summarizes the reviewed literature about the thermal disinfection of various pathogens. Our technology does not directly disinfect the flowing air, and it decontaminates air inside a closed box and inactivates pathogens entrapped within the filter located inside it. Utilizing high temperatures is costly and can burn the filter fiber. Hence, to reduce the operation costs of our system, we opted for using a moderate temperature with a reasonable duration, and based on the previous research, we concluded that utilizing 65°C for 15 minutes will fully inactivate pathogens while it is safe and cost-effective. This conclusion is also supported by the reviews done by Abraham et al. [32] and Kampf [33].

Table 2-1- Summary of temperature and time requirements for inactivating different pathogens

Reference	Pathogen Type	Air flow	Inactivation Temperature	Inactivation time
[22]	MS2	18 l/min 36 l/min	170°C 250°C	0.1~1 s
[23]	SARS-CoV-2	10 l/min	150°C	1.44 s
[24]	SARS-CoV-2, Bacillus anthracis spore	10 l/min	200°C	Single-pass air flow through the heater
[25]	SARS-CoV-2	5000 l/min	150°C	Single-pass air flow through the heater
[26]	Influenza H7N9	-	56°C 65°C 100°C	30 min 10 min 1 min
[27]	Influenza	-	65°C	10 min
[28]	Hepatitis E	-	65°C	1 min
[29]	MERS-CoV	-	56°C 65°C	25 min 15 min
[30]	SARS-CoV-2	-	56°C 65°C 95°C	30 min 15 min 3 min
[31]	SARS-CoV-2	-	60°C	10.5 min
[32]	SARS-CoV-2	-	65°C	5 min
[33]	SARS-CoV Strain Urbani	-	65°C	15 min

2-3- Setbacks of the Reviewed Disinfection Technologies

Although the technologies discussed in the previous section seem to be promising, there are serious setbacks related to them. Some of them lose their efficiency over time, and some others can have health hazards for building occupants by generating harmful by-products in the disinfection process. Thus, they are not fully safe.

2-3-1- Setbacks of Filtration

The filtration approach works quite well at the filters' initial life stages. Nevertheless, after some time, the pores of these filters get filled with particles and pathogens, and they form a layer on the filters. Figure 2-4 illustrates the formation of such layers on the pleats of filters with different pleat angles [34]. These filled porous media block the airflow and cause excessive pressure drop. Considering that filters can contribute up to 50% of the required fan power in a duct system [35], filter clogging highly increases the electricity cost to drive the fan. Therefore, it is required to replace them at the end of their lifespan [36]. Since filters are filled with various particles and pathogens at the filter change stage, any attempt to remove and replace the filter will be dangerous, as it will disturb the pathogens within the filter and expose the person to infection risk. Moreover, the particles accumulated on the filter surface may continue to grow and reproduce, and filter media can be a breeding ground for pathogens [37]. Hence, it is extremely important to devise technologies to inactivate and kill pathogens before removing the filter.

2-3-2- Setbacks of Electrostatic and Biocidal Filters

Reinforcing filters with electrostatic forces or adding biocidal functions also have some problems. Using electrostatic filters adds to filtration costs because of the addition of electrical parts, and it will not solve the pathogen colonization issue in filters. Additionally, using electrostatic technology can produce harmful by-products such as ozone as a consequence of the ionization of some particles, such as volatile organic compounds [7,38]. Furthermore, using biocidal coatings has lower disinfection efficacy for inactivating various pathogens as compared to other rival disinfection methods [39]. Using these materials can also be hazardous, as these coating particles can break up from filter surfaces, travel through the air, find their way to human lungs, and cause health problems [40].

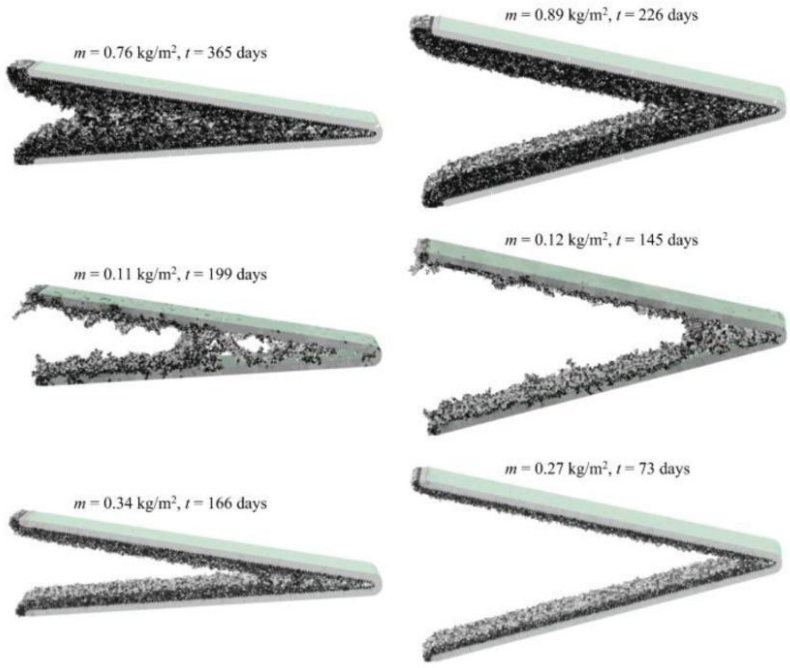

Figure 2-4- Particle accumulation on a filter pleat's surface over time [34]

2-3-3- Setbacks of Ozonation

The ozonation method also has a major setback. Ozone gas is known to be highly hazardous for humans, and it can cause several diseases such as eye irritation, decreased lung function, chest discomfort, and asthma [41]. As ozone is mainly used as a disinfectant material in the ozonation method, it can increase the ozone concentration indoors, reduce indoor air quality, and lead to health problems [12,42]. Due to the remarkable side effects of ozone, the Canadian federal health department, Health Canada, recommends against the use of ozonation-based air purifiers [43].

2-3-4- Setbacks of Ultraviolet Irradiation

Despite its notable disinfection capabilities, UV technology has its limitations as well. UV disinfection strongly depends on the air humidity, and increasing humidity reduces its disinfection efficiency [44]. In addition, the decay rate of different materials accelerates under UV irradiation. Since polymers are highly susceptible to UV decay, UV can damage the ductwork sealing polymer material, and UV radiation can leak to the ambient outside of the ductwork [45]. Since human body is highly sensitive to UV radiation, this UV light leakage can bring about health problems to building occupants. Lastly, the UV disinfection process can lead to ozone and hazardous radicals production that have harmful health effects [46].

2-3-5- Setbacks of Plasma and Photocatalysis

The chemical reactions during the application of plasma and photocatalysis technologies can create some drawbacks. Plasma reactions can lead to harmful ozone or nitrogen oxide production [47]. The photocatalysis method shares the same safety issues, and it can generate hazardous organic or inorganic by-products such as ozone or aldehydes [48].

2-3-6- Setbacks of Microwave and Thermal Inactivation

As mentioned before, microwave disinfection mainly relies on thermal inactivation of pathogens. The thermal inactivation method does not produce any harmful by-products. However, the main issue with microwave inactivation is the capability of particles in microwave absorption [49]. This low absorption rate reduces the efficiency of the microwave approach, and additional microwave absorption materials should be used to increase the microwave absorption rate [50].

The main limitations of thermal disinfection technology are the required temperatures and their corresponding duration for full pathogen inactivation. For example, Grinshpun et al. [22] showed that the required temperature is more than 100°C for single-pass air flow disinfection with an 18 l/min flow rate to guarantee full pathogen inactivation. Additionally, Batejat et al. [30] showed that inactivating the SARS-CoV-2 virus is possible if the air undergoes 30 minutes of heating at 56°C temperature, and this disinfection time can be reduced by further increasing the temperature. Providing and maintaining such high temperatures with a uniform temperature distribution is a costly and formidable challenge. Moreover, disinfecting air with lower temperatures requires more time, and this approach cannot be used if a continuous air flow is desired.

In summary, it can be concluded that the discussed technologies, except thermal disinfection, are not fully safe due to harmful irradiations, hazardous by-products, or low efficiencies. In addition, thermal disinfection requires high temperatures or long disinfection periods to achieve full inactivation. Thus, there is a crucial essence for a reliable technology that is both highly efficient and safe. Table 2-2 summarizes the basic principles of the discussed technologies and the main concerns associated with each of them.

Table 2-2- Summary of the existing disinfection technologies

Technology	Short Description	Main concerns
Filtration	Separates particles and air, entrapping particles in a porous medium [2],[3].	Does not inactivate the pathogens, and particle accumulation on the filter surface increases the required pump power [34–36,51].
Electrostatic filtration	Increases the efficiency by adding electrostatic mechanisms to filter and reduces the pressure drop [7].	Pathogens stay active on the filter surface, and eventually, particle accumulation leads to a rise in pressure drop [7,38].
Biocidal coatings	Biocidal function is added to filters by coating them with antibacterial and antiviral nano materials [8].	Particle accumulation on filter surfaces will lead to excessive pressure drop. The nanomaterial used in the filter surface can enter indoor air and create health hazards for occupants [39,40].
Ultraviolet irradiation	Disinfects the air by irradiating ultraviolet radiation to pathogens [9–13].	It can lead to ozone generation, has radiation leakage risk, and depends on air humidity [44–46].
Ozonation	Reacts with pathogens and inactivates them through oxidization [14].	Increases the ozone concentration in indoor air, which is harmful to human body [41,42].
Plasma	Produces reactive species that react with pathogens and inactivate them [15].	It can generate ozone and nitrogen oxide [47].
Photocatalysis	Irradiating a photocatalyst applied to a surface can generate reactive species that inactivate the pathogens [16].	It can produce organic and inorganic by-products such as ozone and aldehydes [48].
Microwave	Inactivates pathogens by irradiating microwaves to them [17].	Particles have low microwave absorption capabilities, and additional materials should be used to increase the absorption rate [49,50].
Thermal Disinfection	Disinfection is achieved by heating air and denaturing pathogens [18].	Requires high temperatures or long disinfection time [22,30]

2-4- Particle Detachment due to Fluid Flow

Particle detachment from a surface occurs when particles resting on a surface are agitated due to various factors, resulting in the re-entrainment of the particles into the air. When a particle is dormant on a surface under an airflow, adhesion and aerodynamic forces act on it, and in simple

words, if aerodynamic forces overcome the adhesion forces, they can move a dormant particle. Then, this detached particle can follow two scenarios. It can continue its movement on the surface or experience a direct lift force and re-entrain into the air stream. The adhesion forces include gravity, electrostatic, and Van der Waals forces. The aerodynamic forces that lead to particle resuspension can have aerodynamic or mechanical origins. Finally, external forces such as an electric field can affect particle detachment [52].

In the following sections, different parameters that affect particle detachment will be discussed.

2-4-1- Effects of Air Velocity, Humidity, Particle & Surface Properties

To characterize particle detachment from a surface, scientists have done a considerable amount of research. For instance, Liu et al. [53] studied the effect of air velocity, temperature, air humidity, and surface roughness on the resuspension of fungi particles with sizes ranging from 1 to 10 μm from an HVAC duct. Their results showed that the air velocity had the greatest effect on the particle detachment, and raising the air velocity from 0.9 to 2.5 m/s can increase the particle resuspension six times. They also reported that humidity and temperature had negligible effects on particle resuspension.

Additionally, Barth et al. [54] studied the effects of particle size, particle and surface material, surface roughness, and critical velocity on particle resuspension in turbulent channel flows by inducing stepwise growing air velocity. They examined particles with a size range of 3 to 45 micrometers and reported critical velocities for resuspending particles. They found that the required critical velocity for particle resuspension reduces with increasing particle size. Additionally, they reported that the surface roughness did not have notable effects on particle resuspension.

Salimifard et al. [55] studied the effects of relative humidity and air swirl on the detachment of particles such as quartz, dust mite, fur, and bacterial spore-Bacillus thuringiensis from carpet, linoleum, and galvanized metal sheet surfaces. Their experiments revealed that air swirl plays a critical role in their research, and adding only 0.3 m/s swirl to the airflow will increase the resuspension rate by two times. They also highlighted that the hydrophilic and hydrophobic qualities of particles have a significant effect on resuspension. Additionally, they highlighted that reducing relative humidity from 80% to 10% doubles the resuspension of dust mite particles.

Wang et al. [56] investigated the resuspension of KCl particles from a straight ventilation duct surface. They studied the effect of air velocity, particle size on particle detachment from the duct surface and concluded that the resuspension rate was highest for larger particles with higher velocities. They additionally illustrated that the velocities higher than 8.8 m/s cause particles with a diameter range of 0.4 to 10 μm to roll and slide, and it prevents them from re-entraining into the air stream.

2-4-2- Effects of Transient and Turbulent Flows

Due to their chaotic nature and high-velocity gradients, turbulent and transient flows can reintroduce particles into the air as well [57]. The advancement in turbulent flow research has shown that, despite the random nature of turbulent flows, there are consistent geometrical features, called coherent structures, in a turbulent boundary layer, and two of these structures can affect particles in the viscous sublayer and log-law region [58]. An example of these structures can be seen in Figure 2-5.

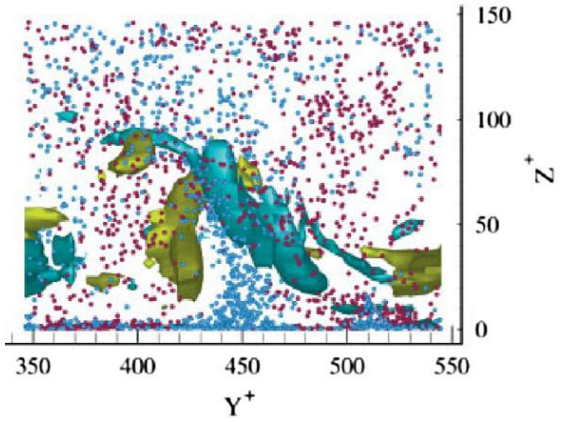

Figure 2-5- Coherent structures present in the vicinity of a wall [58]

The first coherent structure involved in particle resuspension is called sweep (spatially coherent fluid motion with a velocity directed towards the wall), and particles moving in the normal direction to the wall are correlated with this structure. The second one is called ejection (spatially coherent fluid motion with velocity directed towards the bulk of the flow), and particles moving towards the wall are associated with it. Thus, particles near these structures experience velocity fluctuations and are more prone to detachment from surfaces [58].

Various studies have been conducted to research the effect of turbulent and transient flow conditions on particle resuspension. For example, Ibrahim et al. [59] experimentally studied the detachment of micro-sized particles in turbulent flows. They observed that the balance between the aerodynamic drag force and rough-surface pull-offs is the determining factor in particle detachment and reported that particle detachment under accelerating transient airflows was 600% times greater than particle detachment in steady airflows.

In another study, Ibrahim et al [60] also did experiments to observe the effect of airflow acceleration on microparticle detachment. They deposited stainless steel particles on a glass substrate and used airflow with acceleration values ranging from 0.3 to 23 m/s^2 to reach a free stream velocity of 14 m/s. Their experiments revealed that the delay in transition from laminar to turbulent boundary layer reduces particle detachment, and flows having quicker turbulent layer development have larger particle detachment.

Mukai et al. [61] researched the effect of air velocity, particle size, and turbulence intensity on particle resuspension from surfaces, including carpet, linoleum, and galvanized metal sheet with particles having diameters less than 20 microns. They varied the air velocity from 5 to 25 m/s with various turbulence intensities ranging from 9% to 34% in the boundary layer. Their results illustrated a considerable increase in particle resuspension with increasing air bulk velocity, turbulence intensity, and particle size.

Theron et al. [62] studied the resuspension of micro-sized particles in the fan acceleration period in HVAC ducts. By utilizing the hot-wire anemometry method for velocity measurements and image analysis for particle counting, they proposed an experimental methodology and observed the effect of velocity change in the viscous sublayer as well as half channel height on the particle resuspension. Their results show that a significant portion of particles is released during the face acceleration period. Additionally, they pointed out that turbulent kinetic energy can also play a role in the start of particle detachment.

Also, in another study, Theron et al. [63] investigated the temporal evolution of microparticle re-entrainment under transient flows. They researched the time required for the initiation of particle resuspension under transient flows in HVAC ducts and concluded that it is necessary to exceed a certain turbulent kinetic energy threshold to start particle resuspension. Moreover, they highlighted that particle resuspension had the highest rate during the initial stages of the fan acceleration.

2-4-3- Effects of Filtration Pressure

Filtration pressure can also be an affecting parameter in particle capturing. Increasing filtration pressure can reduce the mean free path of the small micro- or nano-sized particles, reduce the Brownian diffusion effects, and increase particle penetration through filters [64]. In this regard, Liu et al. [65] Investigated the effect of changing filtration pressure on particle penetration in glass fiber and metal fiber filters. They did experiments with particles with 20 to 400 nm size ranges and varied the filtration pressure from 0.33 to 3 atm. The results indicated that at a face velocity of 0.1 m/s, increasing pressure from 0.33 to 3 atm increases particle penetration from 0.8% to 14% for glass fiber media (Figure 2-6) and from 6.7% to 32.1% for the metal fiber media. As can be seen in the figure, pressure changes in the order of a few atmospheres are required to have notable changes in the filtration capability of the filter.

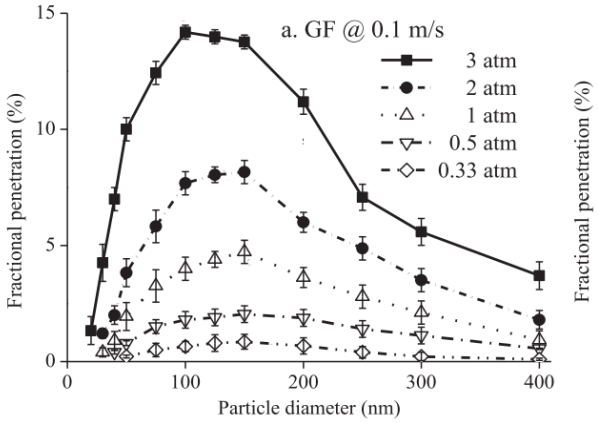

Figure 2-6- Particle penetration of particles with various diameters under different filtration pressures [65]

Furthermore, Xu et al. [66] researched the impact of filtration pressure on the efficiency of F7, F9, and E10 filters. They used particles with a 0.3 to 5 micrometer size range with four face velocities ranging from 3 to 9 m/s and filtration pressures ranging from 60 to 130 kPa to do their experiments. The results indicated that the filtration efficiency for small particles was more sensitive to the filtration pressure change, and changing filtration pressure from 60 to 130 kPa can lead to a 15% reduction in filtration efficiency.

2-4-4- Effects of Vibration and Mechanical Forces

In addition to aerodynamic factors, vibrations and human activities can also play a crucial role in particle detachment from surfaces [52]. For example, Al Assaad et al. [67] combined particle

resuspension models and CFD to observe the effects of mechanical and aerodynamic agitation. By using a probabilistic approach, they coupled CFD and a mathematical model to predict particle resuspension from hard indoor surfaces, which was triggered by vibrations and indoor activities such as walking. They did their research on three surfaces – glass, marble, and linoleum and reported that the resuspension rate was escalated by 63% for the linoleum surface when vibration forces were added to aerodynamic forces.

Additionally, Boulbair et al. [68] did CFD simulations to investigate the resuspension of particles due to human walking. They investigated the impact of walking and shoe groove patterns on the resuspension of particles and realized that stepping creates an air jet under the foot and counter-rotating vortices around the shoe, which can disturb the particles on the floor and eventually resuspend them. Moreover, Benabed et al. [69] experimentally studied the effect of human walking on the resuspension of PM 10, PM 2.5, and PM1 particles from hardwood and linoleum surfaces. Their tests concluded that the resuspension fraction was higher for larger particles, PM10, and the hardwood surface had more particle emission than the linoleum surface, as it has more surface roughness and less adhesion forces acting on particles.

2-4-5- Particle Release from HVAC Filters

Considering the complexities of the adhesion forces acting on a particle in a fibrous filter medium and measuring particle detachment from it, there is limited research done in this area. In this regard, Morisseau et al. [70] researched the effect of relative humidity and fan acceleration on particle release from fibrous filters with five different filtration efficiency classes. They clogged these filters with fungus Penicillium chrysogenum microparticles with diameters around 6 micrometers. After clogging the filters, they put the loaded filters in the test section, started the fan, and let it run for 14 minutes with velocities ranging from 0.13 to 0.21 m/s for different filters. Their results illustrated 0.001% to 1% particle release as a result of the fan acceleration. Moreover, they reported that most of the particles were released in the first 2 minutes of the fan acceleration, which highlights the significant effect of fan acceleration and transient changes on particle release from the filters.

In addition, Jankowska et al. [71] researched the re-entrainment of Penicillium brevicompactum and Penicillium Melini with 2-3 micrometers from filters with F5 and F8 filtration classes. In their experiments, they tested airflows with different speeds in two directions, opposite to and the same direction as the filter loading direction. The results of their experiments showed that there is no

notable change in particle re-entrainment for different airflow directions. Also, they noticed that when the re-entrainment velocity is the same as the loading velocity, the particle release was less than 0.00002%. However, when they increased the velocity from 0.09 to 3 m/s, the re-entrainment increased up to 12%. Thus, they concluded that velocity and acceleration have a significant impact on the particle release.

Table 2-3 summarizes the reviewed literature in this section. It is evident in the reviewed literature that air velocity, acceleration, turbulence, pressure, surface roughness, and particle size and type are affecting parameters in particle release from surfaces and fibrous filters. Thus, it is essential to minimize air velocity, acceleration, turbulence, and pressure on the filter surface to ensure that the aerodynamic forces will not dislodge the particles entrapped within the filters.

Table 2-3- Summary of reviewed papers regarding particle resuspension

Ref.	**Studied parameters**	**Particle size**	**Air velocity**	**Surface type**	**Particle type**
Liu et al. [53]	Air velocity, particle diameter, relative humidity, surface roughness, and air temperature	1- 10 µm	0.3 - 2.5 m/s	plastic, steel	Fungal spores
Barth et al. [54]	Particle size, particle and surface material, critical friction velocity	3 - 45 µm	1 - 10 m/s	Glass, steel	Smooth borosilicate glass, steel
Salimifard et al. [55]	Relative humidity, air velocity	1-20 μm	0 – 2.5 m/s	Carpet, linoleum, galvanized metal sheet	Quartz, dust mite, cat and dog fur, bacterial spore-Bacillus thuringiensis
Wang et al. [56]	Air velocity, particle size	0.4 – 10 μm	3.8 – 8.8 m/s	Stainless steel	KCl salt
Ibrahim et al. [59]	Particle diameter, air velocity	10 – 77 μm	0 – 23 m/s	Glass	Stainless steel, glass, lycopodium spores
Ibrahim et al. [60]	Particle diameter, air velocity, and acceleration	64 - 76 μm	0 – 14.1 m/s	Glass	Stainless steel

Mukai et al. [61]	Air velocity, particle size, turbulence intensity	1- 20 μm	5 – 25 m/s	Carpet, linoleum, galvanized metal sheet	KCl salt
Theron et al. [62]	Air velocity, fan acceleration, and turbulent kinetic energy	3 to 30 μm	0 – 7.6 m/s	Antistatic PMMA	Bronze
Theron et al. [63]	Air velocity, fan acceleration, and turbulent kinetic energy	3 to 30 μm	3 to 9 m/s	Antistatic PMMA	Bronze
Liu et al. [65]	Filtration pressure, particle size, and particle penetration	20 to 400 nm	0.1, and 0.2 m/s	Glass fiber, metal fiber	NaCl
Xu et al. [66]	Filtration pressure, particle size, air velocity, and filtration efficiency	0.3 to 5 μm	3 – 9 m/s	Glass fiber	KCl
Al-Assaad et al. [67]	Vibration, air swirl	2 to 9 μm	0.0135 -1.5 m/s	Glass, Marble, Linoleum	Quartz dust
Boulbair et al. [68]	Human walking pattern, shoe grooving, friction velocity, particle size, particle type, surface type	0.1 to 1 μm	0 to 5.4 m/s	Linoleum, steel	Arizona test dust, polystyrene latex spheres, alumina
Benabad et al. [69]	Human walking pattern, particle size, surface type, part	0.01 to 10 μm	-	Hardwood, linoleum	Al2O3
Morisseau et al. [70]	Air velocity, particle size, filter type, water retention capacity, particle release	6 μm	0.13 to 0.8 m/s	G4, M5, M6, F7 fibrous filters	Micronized rice particles with Penicilium chrysogenum fungal particles
Jankowska et al. . [71]	Air velocity, particle size, particle type, filter type	2.55 to 3.25 μm	0.09 to 3.91 m/s	F5 and F8 fibrous filters	Penicillium brevicompactum, Penicillium melinii, KCl

2-5- Forces Acting on Particles Subjected to Fluid Flow

To characterize the forces acting on a spherical particle in a fluid flow with low density, i.e., the density of the fluid is negligible as compared to the density of the particle, three terms Maxey-Riley equation can be used [58,72,73]. This equation classifies forces acting on a particle F_p as:

$$F_p = F_{PG} + F_{drag} + F_{lift} \quad (1)$$

Each of these forces is explained below

a. F_{PG} is the force applied on the particle by a fluid flow with a pressure gradient present and can be expressed as:

$$F_{PG} = \vartheta_p \rho_f \frac{DV_f}{Dt} \quad (2)$$

In this equation, ϑ_p is the particle's volume, *D/Dt* is the material derivative, that is $D/Dt = \partial/\partial t + \mathrm{V}.\nabla$, V_f is the fluid velocity, and *t* is time [58,72].

b. The third term is the drag force, which stems from the velocity difference between the particle and the flow. By using the basic laws of fluid mechanics, this force can be written as:

$$F_{drag} = \frac{1}{2}\rho_f C_D A_P |(V_f - V_p)|(V_f - V_p) \quad (3)$$

Where C_D is the drag coefficient of the particle, A_P is the cross-sectional area of the particle, and V_f and Vp are the fluid and particle velocities, respectively. These parameters vary based on the particle's shape. Considering a spherical particle, this equation will be

$$F_{drag} = 3\pi d_p \rho_f \nu_f (V_f - V_p) \quad (4)$$

Here, d_p is the particle diameter, ν_f is the kinematic viscosity of the fluid [58,72].

c. The lift force F_{lift} is the force applied to the particle in the direction normal to the flow's direction, and it is dependent on the differences between the fluid and particle velocities as well as the particle's rotation rate. Due to the complex nature of the lift force acting on a particle, scientists have only proposed empirical equations to characterize this force based on the particle and flow properties. For instance, the lift force in a fully turbulent boundary layer can be characterized as [58,72], [74,75]:

$$F_{lift} = \lambda\, \nu_f^2 \rho_f \left(Re_p\right)^{\beta}, \quad (5)$$
$$\begin{cases} \lambda = 20 \pm 1.57,\ \beta = 2.31 \pm 0.02 & 3.6 \le Re_p \le 140 \\ \lambda = 56.9 \pm 1.1,\ \beta = 1.87 \pm 0.04 & 0.6 \le Re_p \le 4 \end{cases}$$

In which λ and β are empirical constants, and Re_p is the particle Reynolds number, which is defined as:

$$Re_p = \frac{\left(V_f - V_p\right) d_p}{\nu_f} \tag{6}$$

These aerodynamic forces act on a particle when there is fluid flow around a particle, and it can be understood that velocity, rate of change of velocity (acceleration), air properties, and particle properties have crucial effects on the aerodynamic forces acting on a particle. The findings in the literature also support that increasing flow acceleration and velocity and changing particle material have substantial impacts on particle release from filters and surfaces.

2-6- Numerical Methods for Simulating Flow Through HVAC Filters

In addition to temperature and time, air flow conditions and pressure drop are also important when it comes to filtration. Since conducting optimization experiments is time-consuming, demanding, and financially expensive, scientists have used CFD simulations to study air flow patterns in the vicinity of HVAC filters. Much research has been done on air flow characterization and pressure drop measurements of HVAC filters with different pleat geometries, such as V- and U-shaped pleats.

Table 2-4 summarizes the research in this field. As can be seen in this table, based on the conditions of the filter and the flow, researchers have adopted various flow models, and they have shown that RANS models, such as standard k-epsilon or k-omega SST, can accurately predict the flow behavior near HVAC filters. Additionally, since modeling the tiny pores of HVAC filters is computationally expensive, researchers have used the Darcy-Forchheimer [53-66] equation to model the porous media rather than modeling the fine fibers. Based on Darcy's law, the pressure drop across porous media in ANSYS Fluent can be characterized as [76]:

$$\Delta P = \frac{1}{2} C_i \rho n V_{filtratopm}^2 + \frac{\mu n}{\alpha} V_{filtration} \tag{7}$$

In the above equation, C_i is inertial resistance, ρ is density, n is porous media thickness, $V_{filtration}$ is filtration velocity, μ is dynamic viscosity, and α is permeability.

Furthermore, most of the research papers have used 2D domains to save computational power without losing much accuracy in the results. Some papers have simulated a single pleat, and some others have further reduced the domain size by simulating only half of a pleat. The schematic of the domain of two of the reviewed papers can be seen in Figures 2-7 and 2-8. Finally, the simulations done in the reviewed literature have used a velocity inlet at the inlet, a pressure outlet at the outlet, and symmetry boundary conditions at the top and bottom of their simulation domains.

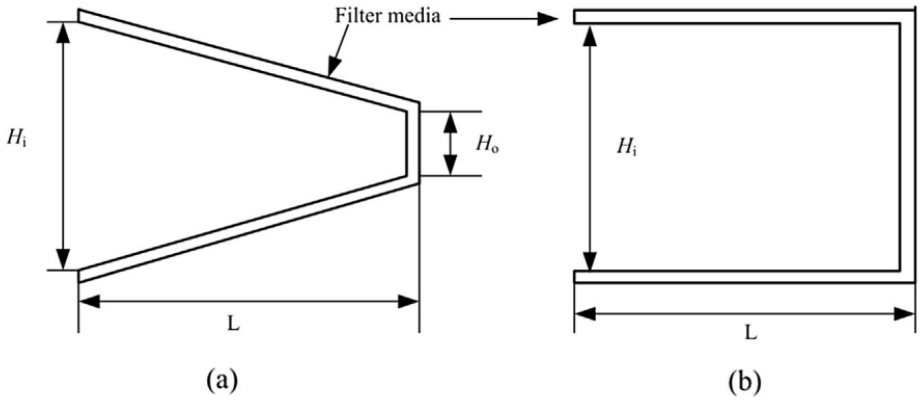

Figure 2-7- The schematic of the numerical domain investigated in Feng's study [77]

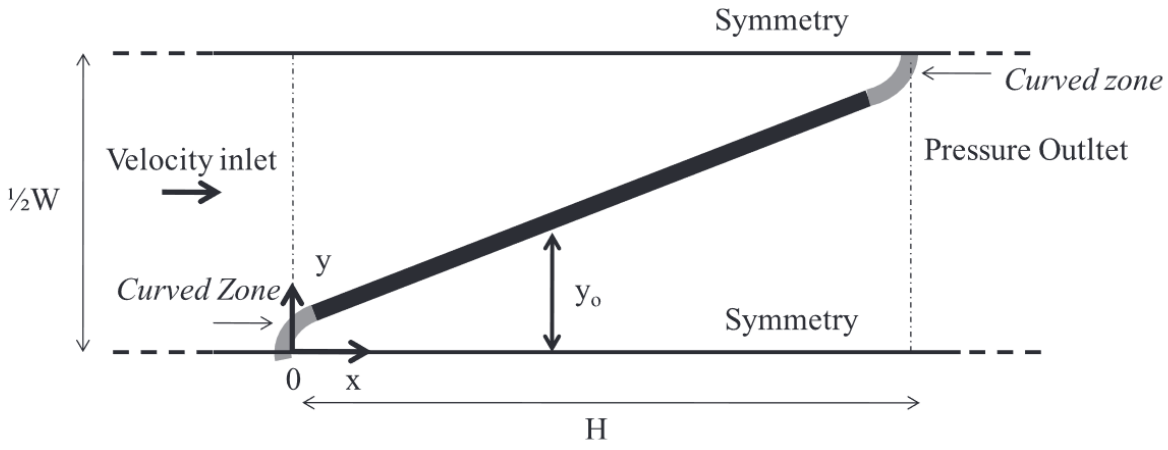

Figure 2-8- Computational domain in Mrad's study [78]

Table 2-4- Summary of the research regarding HVAC filters done by using numerical simulation

Reference	Studied parameters	Filter geometry	CFD domain	Flow Model	Airflow Velocity	Filter material, permeability α (m^{-2})
Zarghanishiraz et al. [25]	- filter layers spacing - particle size - filter efficiency	Interwoven nichrome wires	3D	SST k-omega	V_air= 1.568 m/s	nichrome fiber
Teng et al. [79]	pleat geometry	U, V Pleated	2D - one pleat	Laminar	V_filtration= 4 cm/s	polypropylene microfiber $\alpha = 9.5810 \times 10^{-12}$ (m^2)
Li, et al. [80]	- pleat geometry - velocity - flow Resistance - filter Efficiency	U, V Pleated	2D - one pleat	Laminar	V_filtration= 0.02 – 0.1 m/s	metal fiber $\alpha = 8.561 \times 10^{-12}$ (m^2)
Choi et al. [81]	- pleat geometry - velocity - pleat tip permeability	U, V Pleated	2D - half pleat	RSM	V_air = 0.1 – 0.25 m/s	filter material is not mentioned. $\frac{1}{\alpha} = 1 \times 10^{11} - 1.4 \times 10^{12}$ (m^2)
Mrad et al. [78]	- velocity - pleat curved zone permeability	V-pleated	2D- half pleat	Laminar Standard k-epsilon	V_air=0.67 m/s V_filtration= 0.27 m/s	glass fiber $\alpha = 3.1 \times 10^{-11}$ (m^2)
Roegiers et al. [82]	- pleat geometry - filter thickness	V-pleated	2D	Standard k-epsilon	V_air= 2.5 m/s	carbon filter $\alpha = 2.71 \times 10^{-10}$ (m^2)
Alilou et al. [83]	velocity	V-pleated	2D - one pleat	k-omega SST	V_filtration= 2 cm/s	HEPA filter $\alpha = 1.19 \times 10^{-12}$ (m^2)
Maddineni et al. [84]	pleat geometry	V-pleated	2D - one pleat	Realizable k-epsilon (fluid) v2f (filter)	V_air= 1 – 5 m/s	filter material is not mentioned. $\alpha = 1.875 \times 10^{-11}$ (m^2)
Theron et al. [85]	- pleat geometry - velocity - pressure drop	V-pleated	2D- half pleat	Standard k-epsilon - RSM	V_air= 0.6 – 5.6 m/s V_filtration= 0.09-0.81 m/s	cotton and polyester fiber $\alpha = 10^{-9}$ (m^2)
Hai-ming et al. [86]	- pleat geometry - velocity - pressure drop	V-pleated	2D - four pleats	Standard k-epsilon RNG k-epsilon RSM	V_filtration= 0.45 – 2.25 m/s	Filter material is not mentioned. $\alpha = 11.89 \times 10^{-12}$ (m^2)

Feng et al. [77]	air velocity	U, V Pleated	2D - one pleat	Standard k-epsilon v2f, LES, DES-SA, LRN LS	V_air= 0.13 m/s	HEPA filter – Polypropylene $\alpha = 8.33 \times 10^{-13}$ (m^2)
Fotovati et al. [87]	- filter geometry - filter age - particle size - pressure drop	V-pleated	2D- half pleat	Laminar	V_air= 0.05 – 0.5 m/s	Filter type is not mentioned. $\alpha = 5.01 \times 10^{-10}$ (m^2)
Rebai et al. [88]	- filter geometry - velocity - pressure drop	U, V Pleated	2D- half pleat	Laminar	V_air=0.39 m/s	Filter type is not mentioned. $\alpha = 3.565 \times 10^{-10}$ (m^2)
Tronville et al. [89]	- pleat number - pressure drop - velocity	V-pleated	2D- half pleat	RMS standard k-epsilon RNG k-epsilon	V_air= 0.5 – 2 m/s	Filter type is not mentioned. $\alpha = 7.5 \times 10^{-12}$ (m^2)
Li et al. [90]	- filter height - filter Diameter - flow Resistance - filtration Efficiency	Cylinderical filter with V-shped pleats	3D, axissymetric	k-epsilon	V_filtration= 2 cm/s	metal fiber $\alpha = 5.8 \times 10^{-13}$ (m^2)

2-7- Summary

The reviewed literature indicates that the existing technologies are not fully effective and safe due to various reasons, such as producing hazardous by-products during the disinfection process. Additionally, the time and temperature requirements support the applicability of the strategy suggested in this project, and a 65°C temperature can inactivate most pathogens in an isolated medium in 15 minutes.

Furthermore, it was seen that fluid flows can impose aerodynamic forces on particles and can detach them from filters. The key parameters enhancing particle release were found to be air velocity, turbulence, flow acceleration, pressure, humidity, particle and surface properties, and vibration.

Lastly, it was seen that numerical simulations can be employed to simulate HVAC filters. The filter media can be modeled by using the Darcy-Forchheimer model, and RANS models can be utilized

to simulate turbulent flows passing through the filters. Moreover, 2D models can be used to simulate filters with high accuracy and lower computational cost.

2-8- Research Gap

It is evident in the reviewed literature that the effects of various parameters on particle release from flat surfaces have been extensively investigated. Additionally, there are research findings about particle release from fibrous HVAC filters. Yet, to the author's knowledge, no research has been done on how flow-disturbing objects – such as the gates, which are the focus of this research, or dampers commonly used in HVAC systems – affect the flow characteristics and particle release from loaded filters.

Understanding the aerodynamic effects of these objects is essential because dampers or similar flow-blocking structures positioned upstream of the loaded HVAC filters and equipment can significantly influence particle emission from the filters. Such particle dislodgement poses potential health risks, including pathogenic infections, to building occupants.

Chapter 3- Experimental Methodology & Setup

3-1 Preface

Experiments are an essential part of this thesis, and experimental data will be used for measuring filter properties, validating the numerical model, showing the velocity uniformity, and measuring particle release from the loaded filters. Porous media modeling requires porous media permeability as an input in the numerical model. Thus, it should experimentally be measured. Additionally, to check the velocity distribution, velocity must be measured at different points across the duct cross-section. Finally, numerical methods cannot model particle release from the loaded filters. Thus, particle release from loaded filters will be measured experimentally under different gate rotation periods.

3-2- Experimental Setup Description

The experiments must be designed to measure velocity at various locations and the pressure drop caused by the units. Additionally, the particle release experiments must be designed to measure the particle release of the filters due to gate movement. Thus, designing and assembling the required test setup was necessary.

The required experimental setup and pieces of equipment for this thesis include a wind tunnel, a fan, a HEPA filter, conventional MERV11 HVAC filters, a hot wire anemometry velocity measurement device, a pressure transducer, a scale, microparticles, and two disinfection unit prototypes.

The wind tunnel has a 24” by 24” cross-section and is designed based on the ASHRAE 52.2 standard with the specifications seen in Figure 3-1. The wind tunnel, along with the other equipment, was assembled and installed in the Filtration Testing Lab by the lab team. The completed setup, which includes the experimental equipment, can be seen in Figure 3-2.

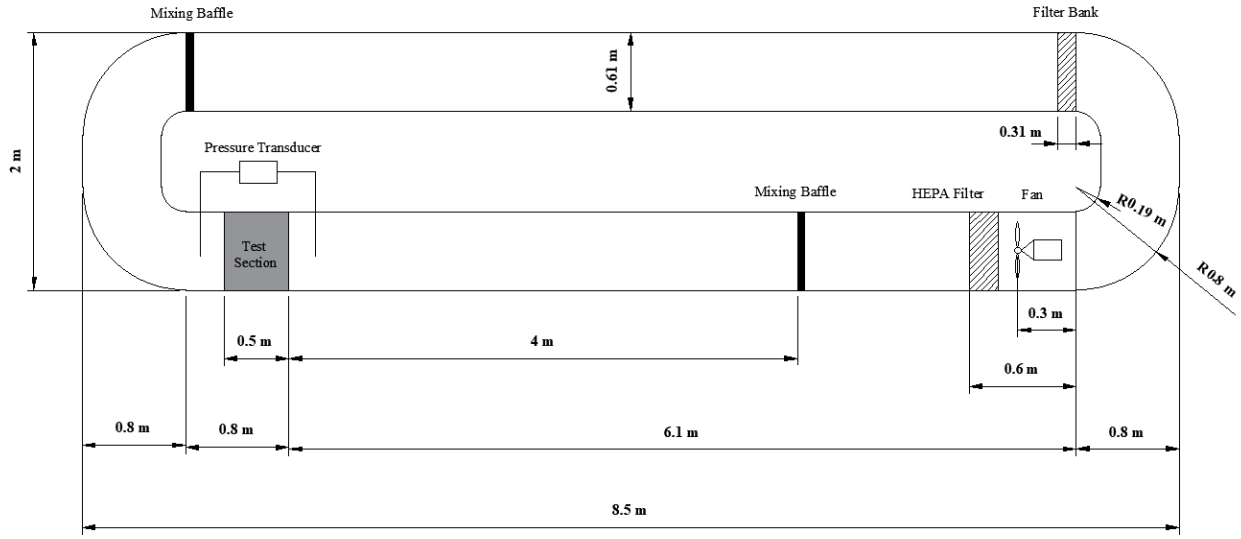

Figure 3-1- Wind tunnel geometry and details

Figure 3-2- Wind tunnel and other experimental equipment

To do the velocity measurements, a TSI 1D velocity measuring device that works based on the hot-wire anemometry method is used (Figure 3-3-a). This device can measure the average velocity within 1s, 5s, 10s, and 30s periods, and report the velocity and air flow values. However, it does not have the capability to report instantaneous velocity values over a period.

The technical specifications of the velocity measuring device are listed below:

- Velocity range: 0 to 30 m/s
- Accuracy: $\pm 3\%$ of reading or $\pm 0.15\ m/s$, whichever is greater
- Resolution: 0.01 m/s
- Response time: 200 msec

Additionally, the Omega PX655-05DI model (Figure 3-3-b) pressure transducer was used to measure the pressure difference between before and after the test section. The technical specifications of this device are listed below:

- Pressure range: 0-5 inches of water column (0-1244 Pa)
- Accuracy: $\pm 0.25\%$
- Repeatability: $\pm 0.05\%$
- Response time: 250 msec

(a) (b)

Figure 3-3- a) TSI hot wire anemometry device for velocity measurements, b) Omega pressure transducer

To carry out the tests, two disinfection units were constructed in the Filtration Testing Lab. These units are illustrated in Figure 3-4.

Figure 3-4- Disinfection unit prototypes

Finally, a Wellish brand scale (Figure 3-5) with an accuracy of 0.001g was used to measure the weight of the particles loaded into the filters and weight loss after the particle release experiments.

Figure 3-5- The scale used in particle release tests

3-2- Key Experiments

The numerical model validation requires experimental inlet velocity and filter medium properties as inputs. Thus, experiments are carried out to measure these parameters. Additionally, particle release experiments are necessary to have a better understanding of the affecting parameters. The details of these experiments are explained in the following sections.

3-2-1- Velocity Profile Measurement

The upstream velocity profile was measured on a horizontal line at the half cross-section height. Since the sampling section was meters away from the fan, it was expected that the upstream velocity profile would be fully developed. However, a mixing baffle was installed close to the test section, and it affected the velocity profile. According to the ASHRAE 52.2 standard, a mixing baffle was designed and used before the data sampling point in the wind tunnel to ensure velocity and particle concentration uniformity across the duct cross-section. Thus, the mixing baffle shown in Figure 3-6 was installed inside the wind tunnel.

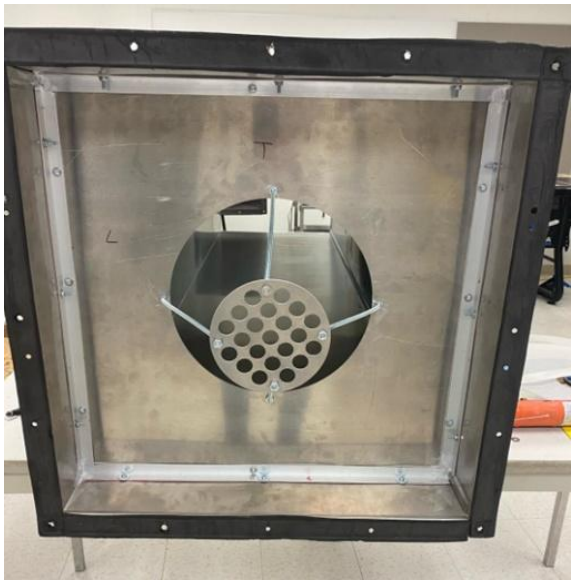

Figure 3-6- Mixing baffle for ensuring velocity and particle uniformity throughout the duct cross-section

After doing some initial tests, it was realized that some changes in the existing experimental setup are required to achieve a uniform velocity distribution. Due to its shape, the mixing baffle was accelerating the flow in the mid-section of the duct cross-section. Since this mixing baffle was close to the data sampling point, the velocity profile at the data sampling point was not fully developed and had a dome shape (Figure 3-7a). Thus, the wind tunnel was opened, and the mixing baffle was moved 1.5 m away from the sampling section. This change resulted in a fully developed velocity profile shown in Figure 3-7b.

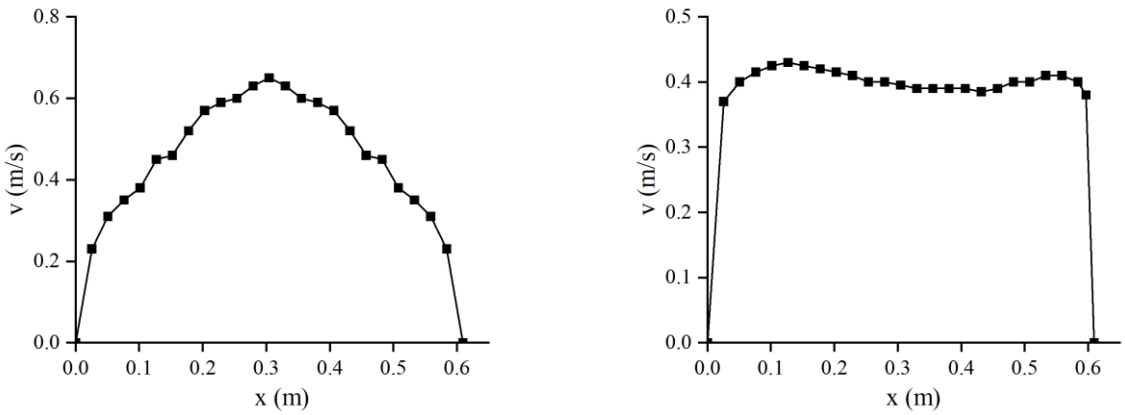

(a) (b)

Figure 3-7- Upstream velocity profile for 509 m3/h (300 CFM) airflow: a) before the mixing baffle relocation, b) after the mixing baffle relocation

3-2-2- Velocity Uniformity Tests

Compliance with the ASHRAE 52.2 standard requires the velocity profile to be uniform at the sampling point. Thus, velocity magnitudes were sampled at 9 points across the cross-section (Figure 3-8). The coefficient of variation (which is the division of standard deviation by mean velocity) of velocity magnitude was less than 4.8% and 2.8% for 472 and 1350 cfm (802 and 2293 m3/h) airflow rates, respectively, which shows that the velocity distribution was uniform. Thus, it can be concluded that the flow was symmetric and two-dimensional.

The data related to the velocity uniformity tests can be found in Appendix A.

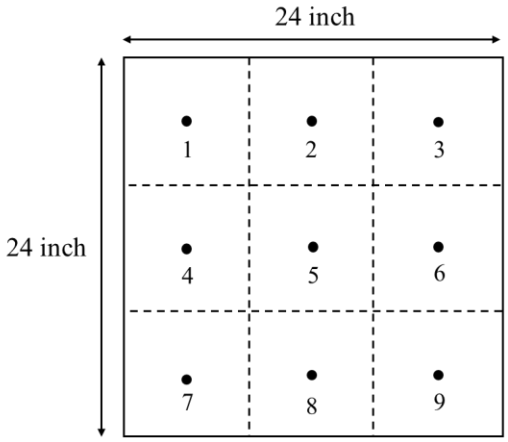

Figure 3-8- Velocity sampling points across the cross-section at sampling location in Figure 3.1

3-2-3- Particle Release Experiments

Three particle release experiments were done with different gate rotation speeds to test whether aerodynamic disturbances might release particles from loaded filters. In these tests, the gates of the units were closed in 10 and 5 seconds, and with a quick shock.

First, the elite clay particles, consisting of particles from various types (Table 3-2), were sieved to get particles with diameters less than 45 micrometers. Then, 20 grams of the sieved particles were manually scattered on the filter surface and smoothly pushed further on the filter with a soft brush. Finally, the loaded filter was placed on a portable air scrubber to suck the air through the loaded filter with a velocity equal to the fan velocity in the wind tunnel to ensure particles on the filter surface deeply penetrate the filter medium. Figure 3-9 illustrates two clean and loaded filters. As can be seen, the particles are scattered uniformly on the filter surface. At the end of the filter loading process, roughly 18 grams of particles were embedded within the filters.

Next, the loaded filters were placed in the disinfection units, the fan was started, and it kept working for 10 minutes so that the transient effects are damped. Then, the gates of one of the units were opened and closed with a constant period 10 times. Between each opening and closing movement, there was a 30-second time gap. This was done because in the real-world application of the system, the gates do not open and close consecutively.

Table 3-1- Composition of the elite clay particles used in the particle release tests

Component	Formula	Percentage
Silica	SiO_2	37.88
Aluminum	Al_2O_3	15.26
Iron	Fe_2O_3	3.13
Calcium	CaO	34.75
Magnesium	MgO	6.27
Sodium	Na_2O	0.07
Potassium	K_2O	2.14
Titanium	TiO_2	0.5

Figure 3-9- clean and loaded filters

After the test, the filter weight loss was measured. This weight loss is associated with the particles released from the filter. These tests were done with a 1614 m3/h (950-cfm) air flow rate, and the experiment with 2s gate movement period was repeated 3 times to check the experiment repeatability. The data related to the repeatability tests can be found in Appendix C.

The results of the particle release tests will be discussed in Chapter 5.

3-3- Filter Properties Calculation

As mentioned in the literature review chapter, researchers have employed the Darcy-Forchheimer model to characterize porous media and to determine porous media properties. Accordingly, Equation 7 will be used to extract the porous media properties.

To do this, the pressure drop vs filtration velocity curve should be plotted, and a second-order polynomial should be fitted to this data. From the fitted equation, the coefficients can be used to calculate the permeability and inertial resistance of the filter medium. Thus, the pressure drops for 8 fan speeds and the corresponding air velocities were recorded, and the air velocity was used to calculate the filtration velocity by using the following equation:

$$V_{filtration} = \frac{Q_{air}}{A_{filter}} \tag{8}$$

In which Q_{air} is the volumetric airflow rate, and A_{filter} is the total area of the filter. To calculate the filtration area, one of the filters was flattened and expanded, and the effective filtration area was measured. The area hidden under the filter frame is not included in the filtration area calculation.

The first step for finding the properties was setting up the pressure transducer and calibrating it, as the output signal received from the transducer was a voltage. The calibration process and the relative data can be found in Appendix B.

After plotting the $V_{filtration}$ vs. pressure drop plot (Figure 3-9), it was realized that the plot is not linear but a curve. Thus, it is concluded that the inertial effects are also significant and should not be neglected.

Table 3-2 lists the air properties used to calculate the porous media properties and the resulting permeability and inertial resistance values. The uncertainty calculations for inertial resistance and filter permeability are presented in Appendix D.

Table 3-2- Properties and the results in porous media properties calculation

Density	1.1614 kg/m³
Filter thickness	0.0005 m
Dynamic viscosity	184.61×10^{-7} Pa.s
Inertial resistance, C_i	378,888 1/m
Permeability, α	192.23×10^{-12} m^2

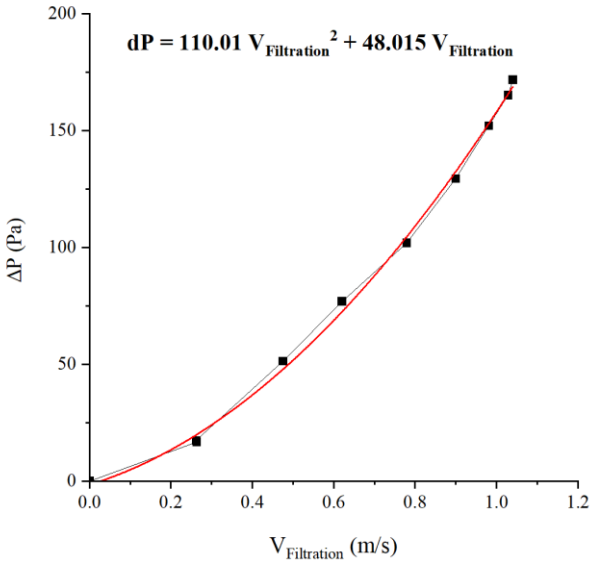

Figure 3-10- Pressure drop vs filtration velocity

3-4- Chapter Summary

This chapter explained the details of experiments and the methods for carrying them out. It was shown that the velocity profile is uniform and fully developed across the duct cross-section at the entrance of the disinfection system. Additionally, the permeability of the filter was calculated experimentally, and the details about the particle release experiments were included.

Chapter 4- Numerical Modeling & Simulations

4-1- Model Development

A numerical model is created to study the effects of gate rotation speed and number of gates on the airflow characteristics during the opening and closing periods of gate movement. The numerical model is created based on the following assumptions:

- The air and filter properties are constant and isotropic because there are no significant changes in temperature or pressure in the airflow. Also, the filter geometry stays steady.
- The flow is 2D. The experimental tests showed that the velocity profile is uniform and fully developed. Thus, considering the geometric and physical symmetry of the system in the vertical direction, the flow is assumed to be symmetric in this direction.
- The external body forces are neglected.
- Flow is turbulent. The corresponding Reynolds number for this flow with 300 CFM ($V \approx 0.4\ m/s$) and 1300 CFM ($V \approx 1.2\ m/s$) is:

$$Re = \frac{\rho V L\prime}{\mu} \approx 16{,}000 \text{ and } 49{,}000 \tag{9}$$

In which Re is the Reynolds number, ρ is air density, V is velocity, L' is characteristic length (the wind tunnel width, 24”), and μ is the air dynamic viscosity. Thus, the airflow inside the wind tunnel is turbulent.

In addition, if the gate’s length is considered as the characteristic length, the Reynolds number becomes 2080 and 6250 for 509 and 2208 m3/h (300 and 1300 CFM) airflows, respectively. These flows can be considered turbulent due to high flow disturbance as a result of gate movement. The significant turbulent kinetic energy growth during the gate movement also proves that the flow is highly agitated and turbulent.

Considering these, the Reynolds number is large enough to assume a fully turbulent flow.

In the following sections, the details related to governing equations, boundary conditions, numerical grid, and solver settings will be discussed.

4-1-1- Governing Equations

The first equation is the conservation of mass. For an incompressible flow, this equation is:

$$\frac{\partial V_{\mathrm{i}}}{\partial x_i} = 0 \tag{10}$$

In equation (10), V_i is the average velocity component, x_i is the Cartesian coordinate system component.

The second equation is the Reynolds-Averaged Navier-Stokes (RANS) conservation of momentum equation [91]:

$$\frac{\partial(\rho V_i)}{\partial t} + \frac{\partial\left(\rho V_i V_j\right)}{\partial x_j} = -\frac{\partial P}{\partial x_i} + \frac{\partial}{\partial x_j}\left[\mu\left(\frac{\partial V_i}{\partial x_j} + \frac{\partial V_j}{\partial x_i}\right) - \rho\overline{V_i' V_j'}\right] + S_i \tag{11}$$

Where ρ is density, t is time, μ is dynamic viscosity, $\rho\overline{V_i' V_j'}$ is the Reynolds stress tensor, and S_i is a source term added to the RANS equation to model porous media based on the Darcy-Forchheimer model. This term for a uniform, homogeneous porous medium is defined as [76]:

$$S_i = -(\frac{\mu}{\alpha} V_i + C_2 \frac{1}{2}\rho|V|V_i^2) \tag{12}$$

In which α is the permeability, and C_2 is the inertial resistance factor.

Since there is flow separation at the locations where gates are located, the k-omega SST turbulence model is adopted because of its high accuracy among the other RANS models. Two additional transport equations, turbulent kinetic energy (k) and specific dissipation rate (ω), are solved in this model [92]:

$$\frac{\partial(\rho k)}{\partial t} + \frac{\partial\left(\rho k V_j\right)}{\partial x_j} = P_k - \beta^*\rho k\omega + \frac{\partial}{\partial x_j}\left[(\mu + \sigma_k\mu_t)\frac{\partial k}{\partial x_j}\right] \tag{13}$$

$$\frac{\partial(\rho\omega)}{\partial t} + \frac{\partial\left(\rho k V_j\right)}{\partial x_j} = \alpha\frac{\omega}{k}P_k - \beta\rho\omega^2 + \frac{\partial}{\partial x_j}\left[(\mu + \sigma_\omega\mu_t)\frac{\partial\omega}{\partial x_j}\right] + 2(1 - F_1)\rho\sigma_{\omega 2}\frac{1}{\omega}\frac{\partial k}{x_j}\frac{\partial\omega}{\partial x_j} \tag{14}$$

Where P_k is the production of turbulent kinetic energy, μ_t is the eddy viscosity, and F_1 is the blending function controlling the model's behavior near walls.

The eddy viscosity μ_t is also defined as:

$$\mu_t = \rho \frac{k}{\omega} \tag{15}$$

4-1-2- Model Schematic and Boundary Conditions

Figures 4-1a and b show the schematic of the numerical model used for this research. The boundary conditions used for this simulation are as follows:

- Constant velocity inlet at the inlet (1% turbulence intensity and 0.61m hydraulic diameter)
- Zero-gauge pressure at the outlet (1% turbulence intensity and 0.61m hydraulic diameter)
- No slip walls on the wind tunnel walls, the filter frame, and the disinfection unit walls

As can be seen, the inlet and outlet boundaries are located sufficiently distant from the critical flow region, i.e., the space between the gates, to avoid numerical errors. In these figures, L is the gate length. Since the particle release experiments were done with 1614 m3/h (950 cfm), the inlet velocity is also set to 1614 m3/h in the main simulations, which corresponds to 1.2 m/s.

The filters are made of 15 pleats of thin fibers with 0.5 mm thickness, 2 cm height, and 2 cm width.

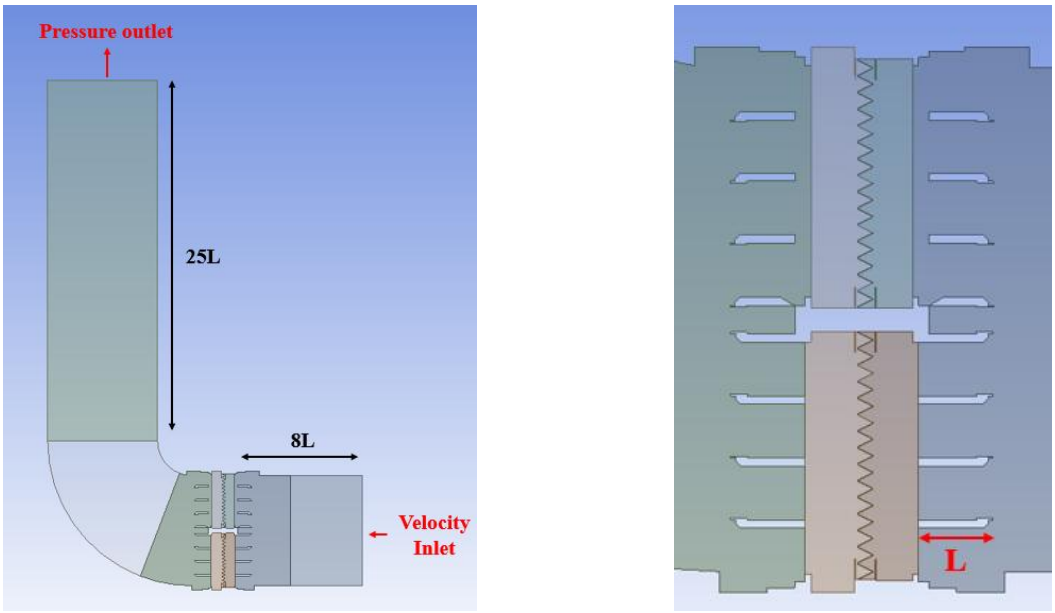

(a) (b)

Figure 4-1- The schematic of the numerical model: a) Complete domain, b) Two side-by-side filters

4-1-3- Numerical Grid

The numerical grid consists of structured and unstructured zones (Figure 4-2). The structured zones include the area in the vicinity of the inlet boundary, the curve after the rear gates, and the area in the vicinity of the pressure outlet boundary. The element size in these zones is 0.005m.

The unstructured mesh includes areas with triangular and quadrilateral elements. The area where the gates are located and the filter area are meshed using triangular elements due to geometrical complexities and dynamic mesh concerns. The area between the gates and the filter is meshed using quadrilateral elements, as the mesh in this area is stationary and non-deforming. The element size for the filter is 0.0004m, for the area between the filter and the gates is 0.001m, and for the area where gates are present is 0.001m. This mesh corresponds to y+ values less than 5 on the gates and the filter frames. Additionally, the majority of the resulting elements have a quality of 0.95 with a skewness of 0.037.

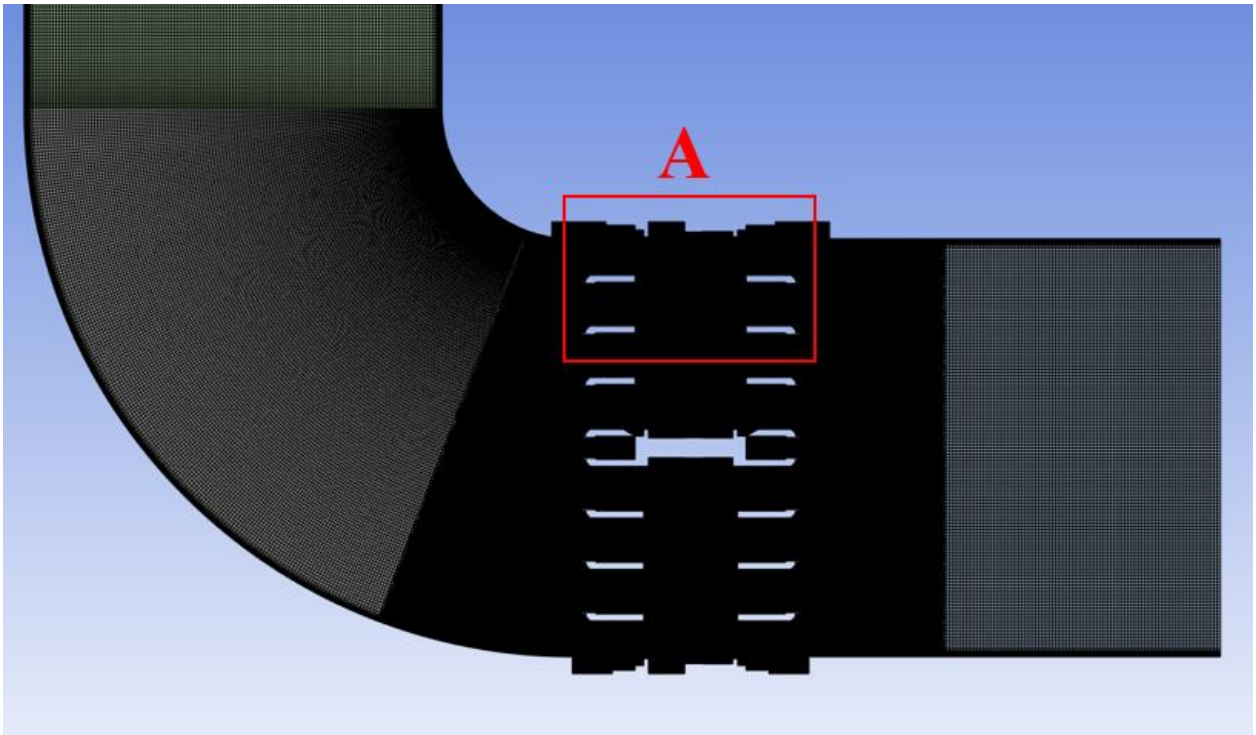

(a)

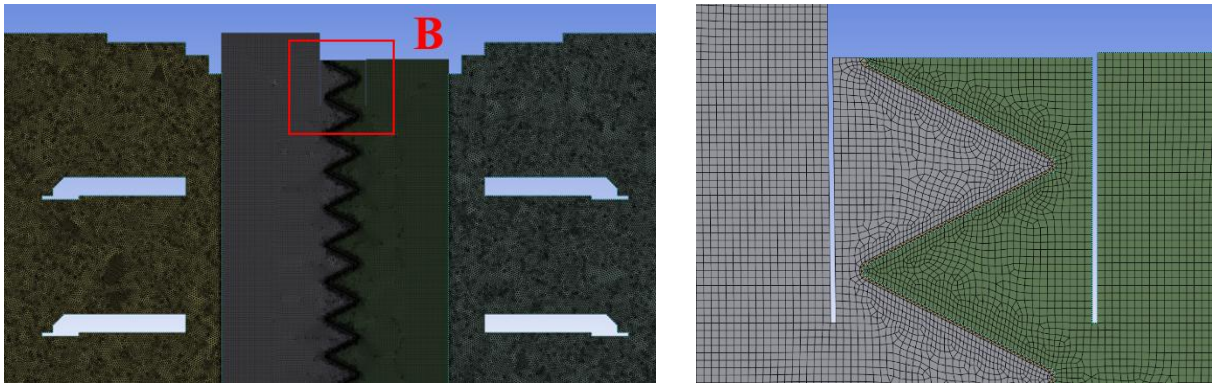

(b) (c)

Figure 4-2- Numerical grid: a) Full domain, b) zoomed view of section A, c) zoomed view of section B

The dynamic mesh imposes some limitations on the mesh generation. Since the gates are moving, the solver must regenerate the deformed and low-quality elements. Regenerating the quadrilateral elements is more difficult and time-consuming than the triangular elements. Thus, the triangular elements are used in the dynamic zone. Furthermore, the inflation layers are not used around the gates because at the end of the gate closing or the beginning of the gate opening movements, the gap between the gates becomes so tiny, and generating inflation layers in these locations will substantially reduce mesh quality. Also, the inflation layers would collapse with the nearby gates, and mesh regeneration would not be possible. Thus, fine elements are used in the dynamic region to ensure high-quality element regeneration while keeping y+ values at satisfactory levels.

4-1-4- Dynamic Mesh Setup

Diffusion and remeshing options are activated to adjust the mesh as the gates move. The diffusion parameter is set to 1.5 to make sure the movement of the mesh in the dynamic zone will be diffused within the triangular mesh zone, and the following settings in the remeshing technique are used:

- Minimum mesh size: 0.0005 m
- Maximum mesh size: 0.002 m
- Maximum skewness: 0.5
- Remeshing intervals: every 5 time steps

During the gates' movement period, if any of the above conditions are not satisfied, Fluent has to re-mesh the deforming domain to comply with the conditions. As can be seen, the mesh size is limited in the 0.0005-0.002 m range to ensure the domain size and quality stay satisfactory with a reasonable flexibility.

Moreover, the rotation speed of the gates is set by defining the gates as moving rigid bodies. Two user-defined functions, one for gates at the front and one for the gates at the back of the unit, are used to define the motion of the gates. These user-defined functions can be found in Appendix E.

4-1-5- Solver Setup

The Ansys Fluent 2023 R3 solver was used to discretize and solve the governing equations. The second-order upwind discretization method was used to increase the stability and accuracy of the solution. Additionally, the coupled scheme was used to ensure the best coupling between velocity and pressure and reduce the iterations required to reach convergence. The residuals of the simulation were set to 1e-6, and the simulation continued until the residuals became stable and numerical and physical convergences were achieved. Finally, the Digital Research Alliance of Canada, formerly known as Compute Canada, clusters were utilized to carry out the simulations. The slurm script and the journal file codes used for setting up the simulations at the clusters are included in Appendix F.

4-2- Model Validation & Sensitivity Analyses

Considering the complexity of the system and the fact that small details can have large effects on the flow behavior, the validation process is done in two steps to understand the affecting factors of the system. First, only the filters are modeled as porous media to ensure that the porous media modeling is correct. Next, the actual system that includes gates and filters is simulated and validated.

Moreover, grid size and time step can have notable effects on the results. However, ultra-fine grids and time steps can substantially increase the required computational power. Thus, the sensitivity of the results to the grid size and time step will be studied as well.

4-2-1- Porous Media Modeling Validation

At this stage, only two side-by-side 12” by 24” filters without the disinfection units were installed inside the wind tunnel (Figure 4-3) to gather experimental data for comparison with the numerical data, and the fan was set to deliver 509 and 2208 m3/h (300 and 1300 CFM) airflows. Additionally, four horizontal rods were installed between the filters and the filter frames to avoid filter deformation under high airflow.

Then, the steady-state inlet velocity profiles upstream of the filters were measured 15cm away from the filters’ front and rear sides at the half wind tunnel cross-section height. A user-defined function (can be found in Appendix E) is written to use the experimentally measured upstream velocity

profiles as the inlet velocity profile in the software. The upstream velocity profiles are plotted in Figures 4-4a and b.

Figure 4-3- Two side-by-side filters installed in the wind tunnel

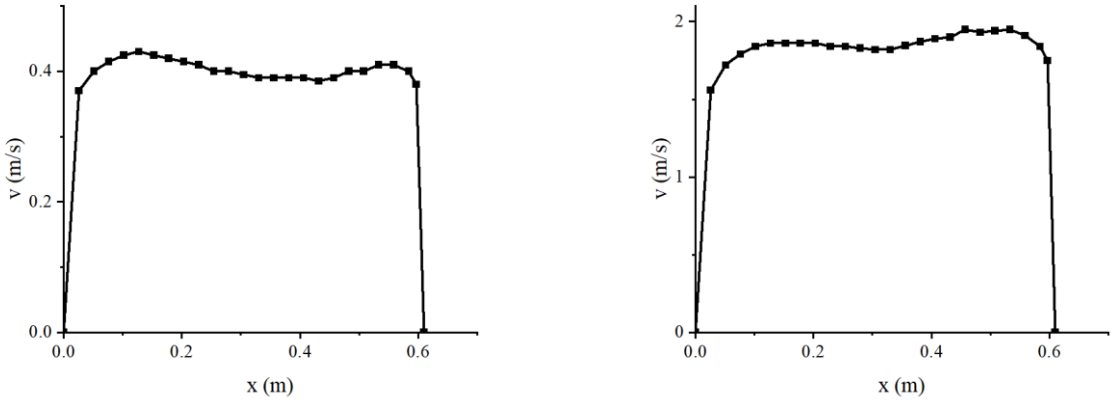

(a) (b)

Figure 4-4- Experimental upstream velocity profiles: a) 509 m3/h, b) 2208 m3/h

In the next step, these filters are modeled in Ansys Fluent. Figure 4-5 shows the schematic of the numerical model, which is created based on the actual wind tunnel and filter dimensions. For validation, the resulting velocity profile 2 cm downstream of the filter (on the red line in Figure 4-5b) is measured in the simulation and compared with the experimental data.

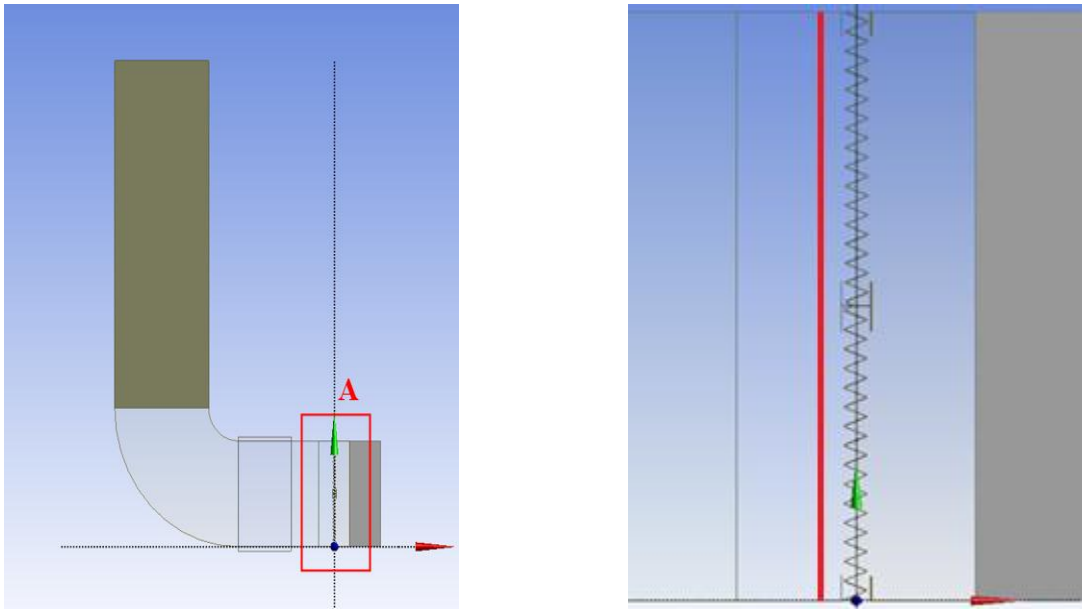

Figure 4-5- The schematic of the porous media validation numerical domain: a) full domain, b) zoomed view of section A

The resulting air velocity field is illustrated in the velocity contours of Figure 4-6. This figure shows that the tiny gap between the filter frame and the filter at the sides and middle sections of the cross-section accelerates flow towards the middle of the filter and has substantial effects on the airflow pattern.

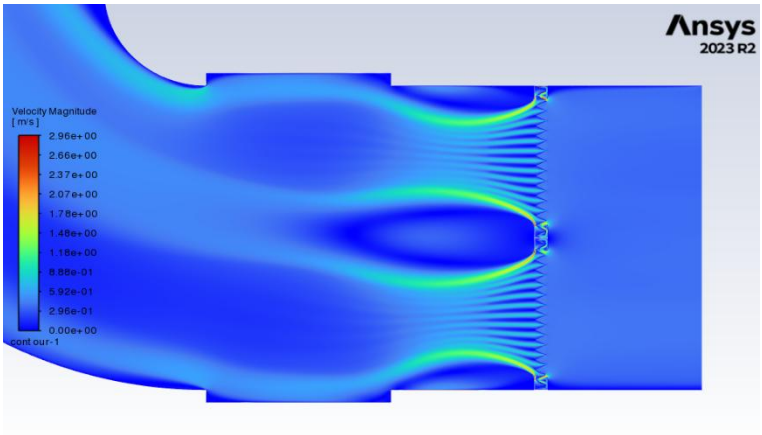

Figure 4-6- Velocity contours of the airflow passing the filters

Figures 4-7a and b show the comparison between the resulting numerical and experimental velocity profiles 2cm downstream of the filter. It can be appreciated that the numerical simulation captures the pattern of the experimental results. Additionally, there is good agreement between the velocity magnitudes.

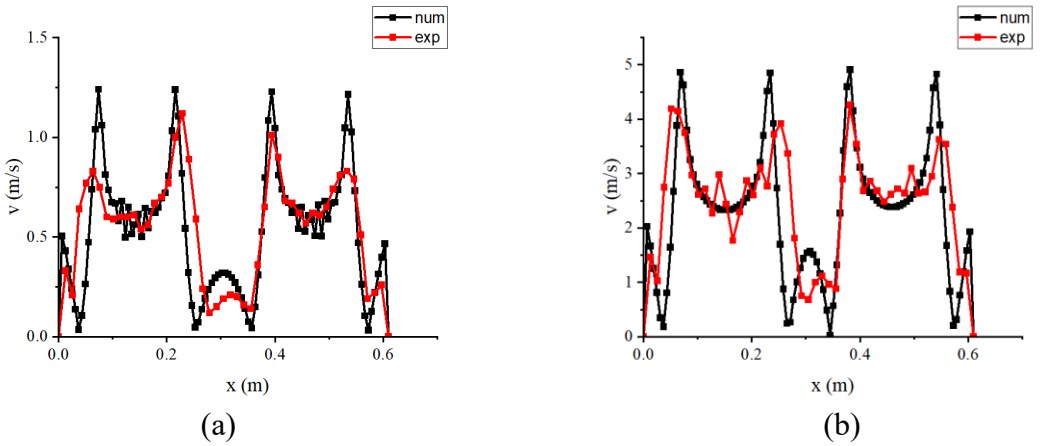

Figure 4-7- Comparison between experimental and numerical results for two air flows: a) 509 m3/h, b) 2208 m3/h

The largest difference between the results occurs in the peaks of the plots. This can be due to several reasons. The first reason is the deformation of the filter frame. Because it is made of a thin 1 mm-thick paper, it deforms under airflow, and the gap between the filter and the frame gets wider. Thus, the airspeed reduces. Therefore, the peaks in the experimental plot are lower than the peaks in the numerical plot. In addition to the filter frame, the filter pleats deform under air flow. In the numerical model, the pleats are modeled as V-shaped structures. In the experiment, however, the straight lines of the V-shaped pleats can be bent and deformed.

Furthermore, the velocity probe has a frame on its sides and can only measure the horizontal velocity. As can be seen in the contour plot, Figure 4-6, there are vortices present in the sides and middle section of the velocity sampling location (15cm away from the filter). Thus, due to the vortex stretching phenomena, velocity has a vertical component too, and 3D factors can be effective where vortices are present.

Taking all these into account, it can be concluded that the numerical model still yields acceptable results, and the model can predict the porous media behavior in the system.

4-2-2- Validation of the Full System

After obtaining the porous media validation, the actual system with two side-by-side disinfection units containing filters is modeled. Figure 4-8 shows the domain of this simulation. As can be seen, one of the units was kept open while the other one was half open.

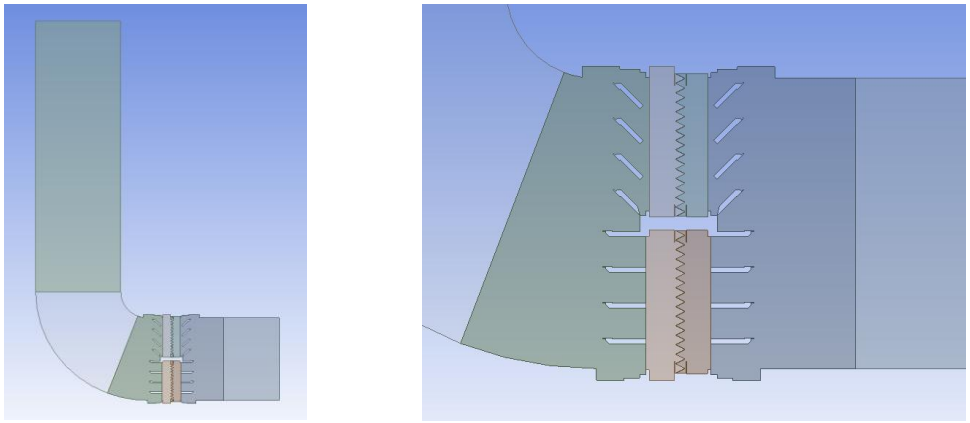

(a) (b)

Figure 4-8- The schematic of the numerical domain for the validation of the full system

Similar to the previous stage, the experimental data at the upstream and the downstream of the units were gathered and compared to the numerical data for 509 m3/h (300 CFM). The comparison in Figure 4-9 indicates that the numerical data overlap with the experimental data and follow the same pattern for both units.

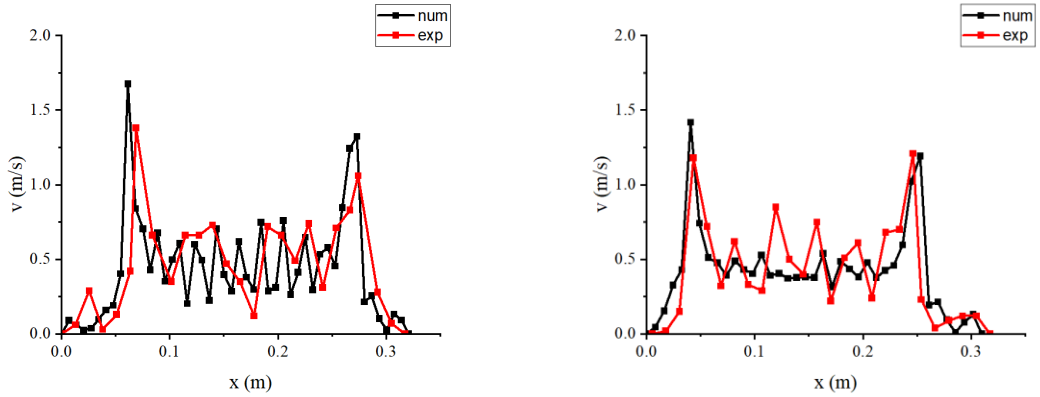

(a) (b)

Figure 4-9- The velocity profiles after filters at 509 m3/h for: a) the unit with open gates, b) the unit with half-open gates

There are also fluctuations in the mid-sections of the filters, which can be attributed to the expansion of the pleats under air pressure and the anisotropic nature of the filter fiber. However, the errors can be explained and ignored since the simulation captures the flow behavior in most of the domain, and it follows the velocity profile trend. Thus, it can be concluded that the assumptions and the simplifications are reasonable, and the numerical model can predict the flow behavior with satisfactory accuracy.

4-2-3- Grid Independence

To ensure the results are independent of the grid size, systematic and uniform mesh refinement was performed, and the number of elements was doubled in each case. Since in the upcoming parts of this research, average flow features on the filter surface will be used, the difference between the average velocity values on the filter surface and the pressure drop across the domain were used to compare the results when the inlet velocity was 1.2m/s.

Table 4-1 shows the results of the grid independence check. Also, Figure 4-10 plots these results. As can be seen, the results become independent of the mesh size as the mesh is refined. Considering the high computational cost and the small difference between cases 3 and 5 (3% difference in V_{ave} and 0.4% difference in dp), the mesh in case 3 is chosen to do the main simulations.

Table 4-1- Grid independence study summary

Case	Element #	V_ave (m/s)	Error (%)	ΔP (Pa)	Error (%)
1	211098	0.74		64.27	
2	468283	0.72	-3.33	63.42	-1.32
3	1041127	0.82	14.56	85.74	35.19
4	2187352	0.80	-2.72	84.78	-1.12
5	5116202	0.79	-0.58	85.42	0.75

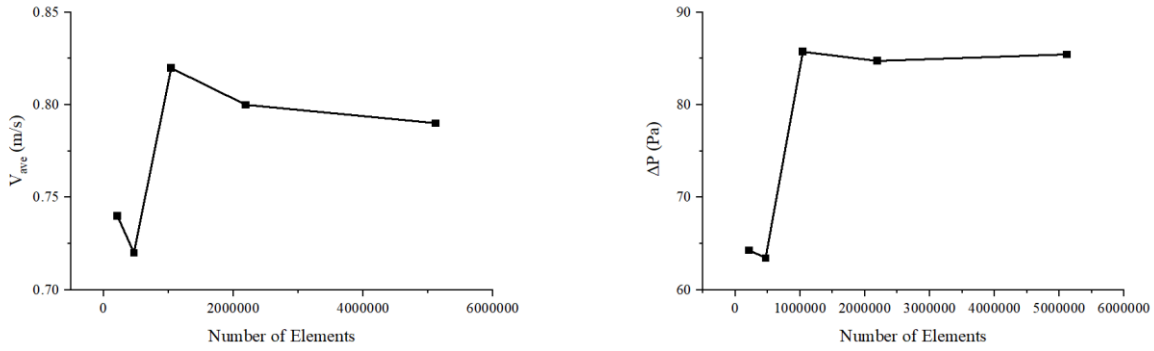

Figure 4-10- Grid independence study results: a) average velocity on the filter surface, b) pressure drop across the domain

4-2-4- Time Step Sensitivity Analysis

Four time-step sensitivity tests were done to select the best time step. A fine time step would yield accurate results; however, it would also increase the computational cost. Thus, the ideal time step must have a good accuracy-computational power balance. A simulation in which the gates get

closed in 2 seconds was done with four different time steps, and the average velocity on the filter surface over time was monitored.

The results of this time step sensitivity test can be seen in Figure 4-11. It is observed that as the time step is refined, more fluctuations are captured and differences occur in the mid-period of the gate movement, especially between 0.5 and 1.8 seconds. However, the difference between the last two fine time steps in this time window is less than 8%. Considering the significant computational power required for this time step, the 0.001s time step is selected for carrying out the main research simulations.

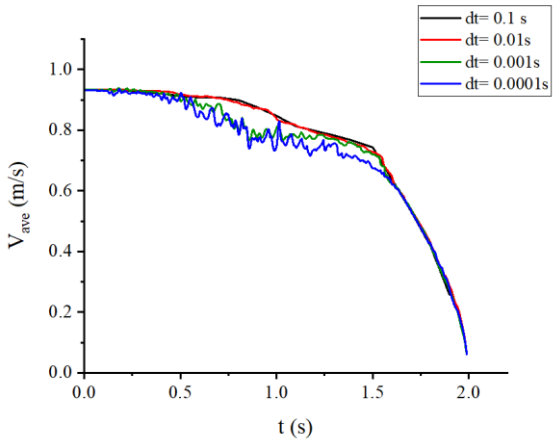

Figure 4-11- Time step sensitivity analysis curves

4-3- Main Simulation Cases

The main simulations can be categorized into two groups: simulations with different numbers of gates and simulations with different gate rotation periods. For the first group, configurations with 1, 2, 3, and 4 gates on each side of the unit will be simulated. Also, the second group involves simulations of the configuration with 4 gates, with 0.25s, 2s, and 10s gate movement periods. Moreover, the opening and closing movements of the gate can yield different results. Thus, each configuration is done for both opening and closing scenarios.

The results of these simulations and their effects on the objective flow parameters will be plotted and discussed in the next chapter.

4-4- Chapter Summary

This chapter outlined the assumptions, governing equations. A suitable 2D model with the exact dimensions of the experimental setup was created and meshed. The solver settings were also explained.

The created numerical model was validated against the experimental data, and a satisfactory agreement between the numerical and experimental results was achieved. Finally, the time step and grid size sensitivity analyses were carried out, and grid and time step sizes were selected.

Chapter 5- Results & Discussion

5-1- Preface

In the following parts, the results of the simulations with different numbers of gates and gate rotation periods will be illustrated. As previously mentioned in the hypothesis section, acceleration, velocity, turbulence, and pressure have adverse effects on the filters, and they can increase the aerodynamic forces acting on the particles. Thus, these parameters are monitored on the filter surface in the simulations, and they are compared to each other.

The domain and mesh configurations were kept the same in the simulations. Additionally, to investigate the effect of the gate movement on the flow, one of the disinfection units was kept open while the other one's gates were opened and closed in the simulations.

Four configurations with 1, 2, 3, and 4 gates were studied to observe the effects of changing the number of gates in front and back of the disinfection units. Moreover, simulations with 3 different gate rotation periods were carried out to see the impact of gate rotation speed. Two simulations are done for each case, when the gates are opening and when the gates are closing.

5-2- Simulations with Different Numbers of Gates

Figure 5-1 displays the velocity contours of the simulations with different numbers of gates when the gates are opening. The results reveal that the flow structures and vortex formations within the unit vary significantly depending on the number of gates. The 1-gate configuration has only one narrow air passage during the early stage of the gate movement. Thus, air is forced to pass through this passage, leading to the creation of a large vortex during the gate movement. This vortex persists throughout most of the gate movement and indicates a strong and continuous flow disturbance, which can contribute to higher turbulence and unsteady acceleration fields.

In contrast, the multi-gate configurations display more complex but less intense vortices. Having multiple openings allows these configurations to have a more uniform flow within them, and although vortices are present in them too, they are smaller and dissipate faster than the vortex present in the 1-gate configuration.

These observations suggest that increasing the number of gates can lead to a more uniform flow while reducing the severity and duration of the vortices created during the gate movement. In the

next sections, the effects of these flow structures and differences on the key parameters are discussed.

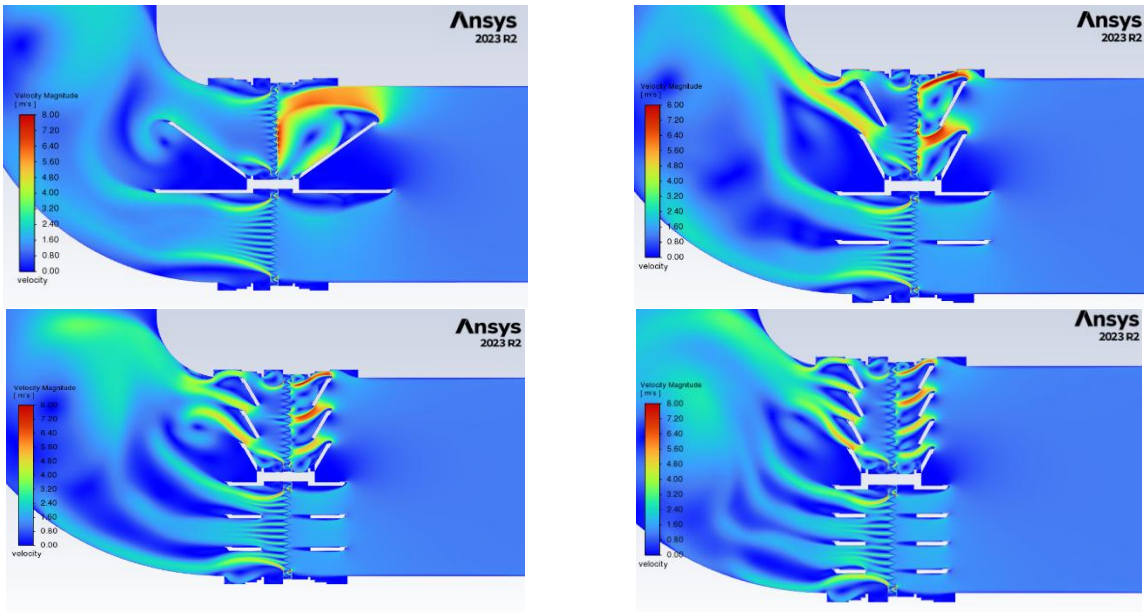

Figure 5-1- Velocity contours of the model with different gate numbers

5-2-1- Effects of the Number of Gates on Average Velocity and Acceleration

Figures 5-2a and b show the average velocity magnitude on the filter surface over time when the gates open and close. It is seen that configurations with 2,3, and 4 gates have almost the same velocity development pattern in both scenarios. In contrast, the 1-gate configuration results in higher average velocity values when the gates are closing and a delay in average velocity development when the gates are opening.

These differences are attributed to the aerodynamic effects of the number of gates on the flow. It was previously seen in velocity contours that during the gate movements in the 1-gate configuration, a single dominant vortex is created at the downstream of the gate, which gradually dissipates. However, multiple gates and openings lead to a more uniform flow distribution and stable development. Thus, the average velocity on the filter surface exhibits the same pattern for the configuration with +2 number of gates, with minor differences. Additionally, the jump and delay in the average velocity pattern in the 1-gate configuration have to do with the gradual creation and decay of the dominant vortex.

From the average velocity results, it can be inferred that the 1-gate configuration performs worst during gate closing movement, as the larger velocity values will result in larger drag forces on the

particles and higher particle release chances. Although the 1-gate case initially lags in velocity development during gate opening, it accelerates fast and eventually reaches the same final velocity as the other configurations. Therefore, in the critical high-velocity phase, all configurations are expected to generate similar aerodynamic forces and potentially similar particle release behavior.

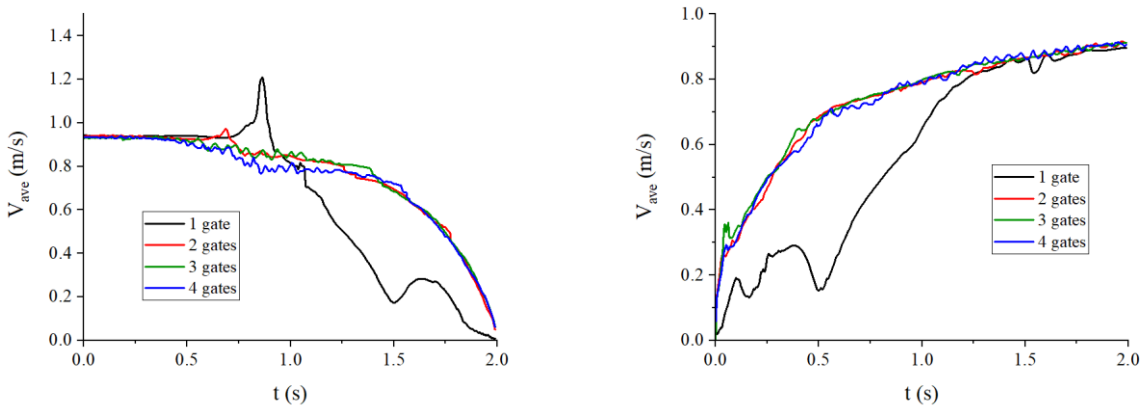

Figure 5-2- Average velocity values on the filter surface over time: a) gate closing, b) gate opening

Flow acceleration is also crucial when it comes to the loaded filters, as it increases the inertial forces on particles within the filters. The temporal acceleration is also calculated to compare the four configurations and inertial effects when the gates open. The acceleration at each time step was computed using the following finite-difference formulation:

$$a^n = \frac{V_{ave}^{n+1} - V_{ave}^{n}}{\Delta t} \tag{16}$$

In which n is the time step.

The resulting acceleration plot is shown in Figure 5-3. The plots show a considerable amount of fluctuation, likely due to the unsteady flow and fluctuating velocity components or numerical noise. Thus, the average acceleration values are compared to have a better comparison between the four cases in Figure 5-4. As expected, the gates with +2 number of gates have similar average acceleration values, but the 1-gate configuration yields a 12% higher average acceleration.

Notably, Figure 5-2b highlights that the largest gap between the 1-gate configuration and the others occurs between 0.5 and 1.5 seconds. When the velocities at t=0.5 and 1.5s are used for the average acceleration calculation in this range, the 1 gate configuration yields an acceleration of **0.71 m/s²**,

whereas the 2+ gate configurations yield only **0.18 m/s²** acceleration values. This represents nearly a **300% increase** in acceleration for the 1-gate case.

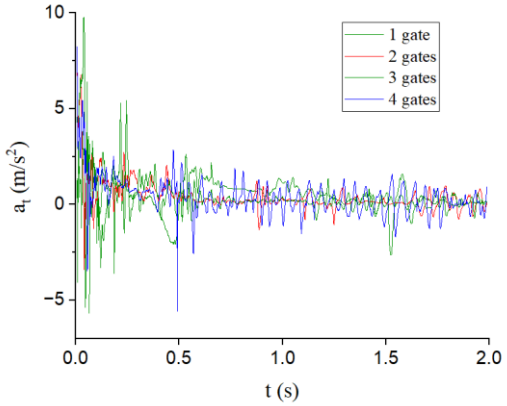

Figure 5-3- Acceleration vs time for the simulations with different numbers of gates

These findings indicate that the 1-gate configuration not only underperforms in terms of average velocity but also exhibits significantly higher unsteady temporal acceleration. These conditions are more likely to increase particle release from the filter.

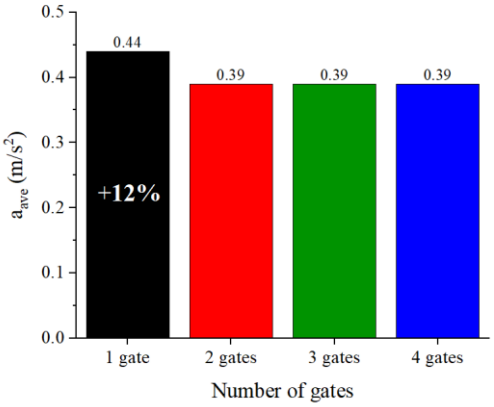

Figure 5-4- Average accelerations for the gate opening movement

5-2-2- Effects of the Number of Gates on Maximum Velocity

The previous section mainly discussed the average velocity values on the filter surface. Since the velocity is directly proportional to the drag force on the particles, the maximum velocity on the filter surface is also monitored when the gates. Higher peak velocities can lead to stronger localized forces, which makes the filter more prone to release particles. Figures 5-5a and b demonstrate this parameter for the gate closing and opening scenarios.

It is evident in these plots that the 4-gate configuration performs better than the other configurations, as it yields consistently lower maximum velocity values. Additionally, it is seen that other configurations result in peak velocity spikes and unsteady behavior throughout the gate movement period. This emphasizes a more uniform velocity distribution in the 4-gate configuration.

The maximum velocity values corresponding to each configuration are compared in Figure 5-6. The comparison demonstrates a **16% and 27% reduction** of the maximum velocity for the 4-gate configuration as compared to the peak values in the chart. Thus, it is concluded that the 4-gate configuration yields both lower average velocity and maximum velocity on the filter surface, which are crucial in minimizing the drag force on the particles within the filters.

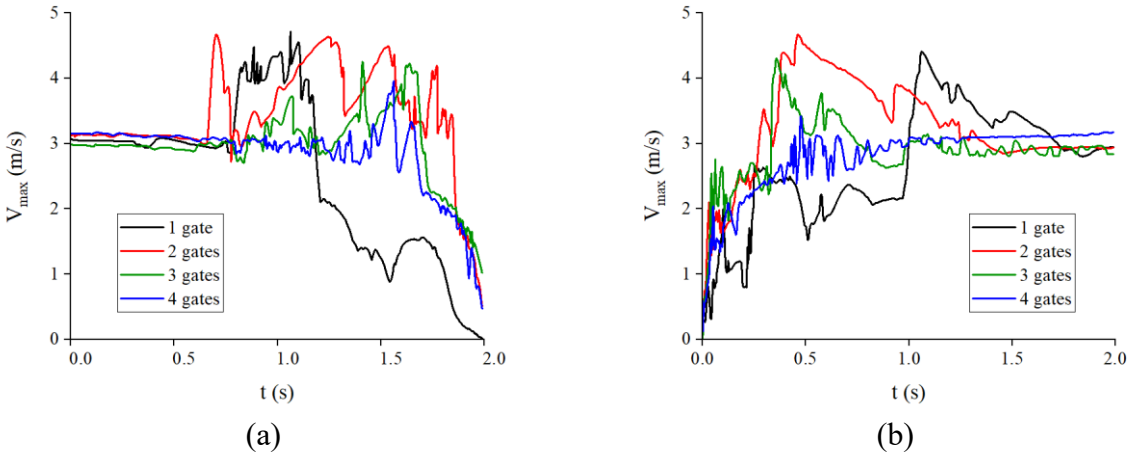

Figure 5-5- Maximum velocity on the filter surface: a) gate closing, b) gate opening

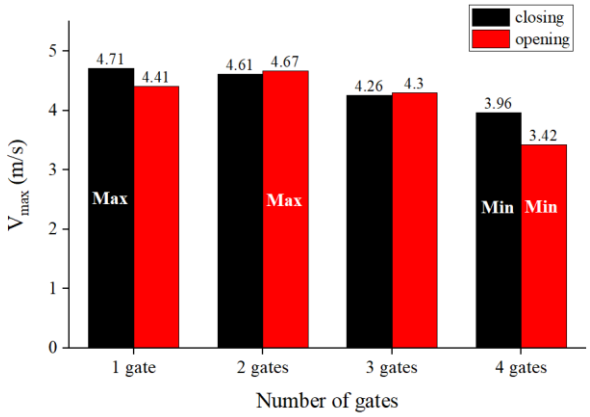

Figure 5-6- Comparison of the maximum velocity on the filter surface for different numbers of gates

5-2-3- Effects of the Number of Gates on Turbulence

As previously observed in the velocity contours, the number of gates significantly influences the flow structure and vortex formation, which affects turbulence conditions as well. Thus, the average turbulent kinetic energy (TKE) was monitored on the filter surface to quantify and compare the four cases. The results are plotted in Figures 5-7a and b for the gate closing and opening scenarios, respectively.

The results demonstrate that the 1-gate configuration exhibits the highest TKE values among the other configurations, as it has the largest vortex formation and flow recirculation during the gate movements. Also, 2-, 3-, and 4-gate configurations have the same TKE evolution pattern due to the similarities between the flow behavior downstream of the gates. Additionally, multiple openings yield better vortex distribution and smaller vortex generation.

The comparison of the peak TKE values can be found in Figure 5-8. It is observed that TKE consistently reduces as the number of gates increases. The 4-gate configuration has the smallest amount of turbulence among the others, owing to smaller and more distributed vortices. Also, this configuration has **89% and 45% lower peak TKE** values compared to the maximum values in Figure 5-8 for closing and opening movements, respectively. From the performance perspective, it is concluded that the 4-gate configuration is superior, as it yields a more uniform and lower turbulence generation.

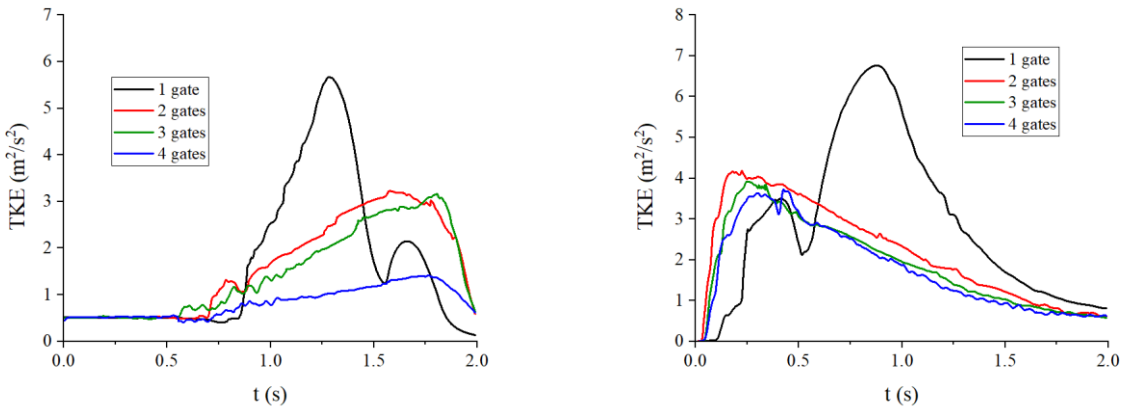

Figure 5-7- TKE evolution during the gate movement: a) gate closing, b) gate opening

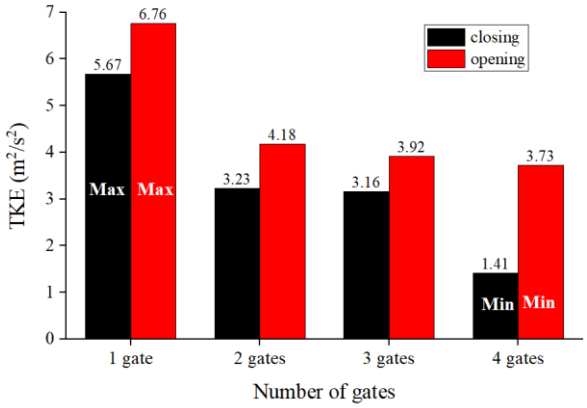

Figure 5-8- Comparison of the peak TKE values for the four configurations

5-2-4- Effects of the Number of Gates on Pressure

Finally, the effect of the number of gates on the total pressure on the filter surface is measured and reported in Figure 5-9. It is seen that when closing the gates, the total pressure reaches 1030 Pa, while the other configurations reach almost similar pressure values, 242 Pa. Thus, the 1-gate configuration results in an almost 4 times greater pressure value on the filter surface.

In the gate opening case, the 1-gate configuration has a different trend, too. Interestingly, the 1-gate configuration yields negative pressure values on the filter surface at the initial moments of the gate opening, as a large body moves fast in a short time. However, the other simulations have the same trend with small differences, and they do not create cavities because of the presence of multiple air inlets to the system.

It can be concluded from the pressure plots that the 1-gate configuration has the worst performance among the others regarding pressure. It was seen in the literature that high pressure reduces the fibrous filters' capability of capturing particles. It is observed that the 1-gate configuration has the highest pressure among the others when the gates are closing. Moreover, in the gate opening case, the results show that the 1-gate configuration creates a cavity inside the unit, which can increase disturbances on the particles.

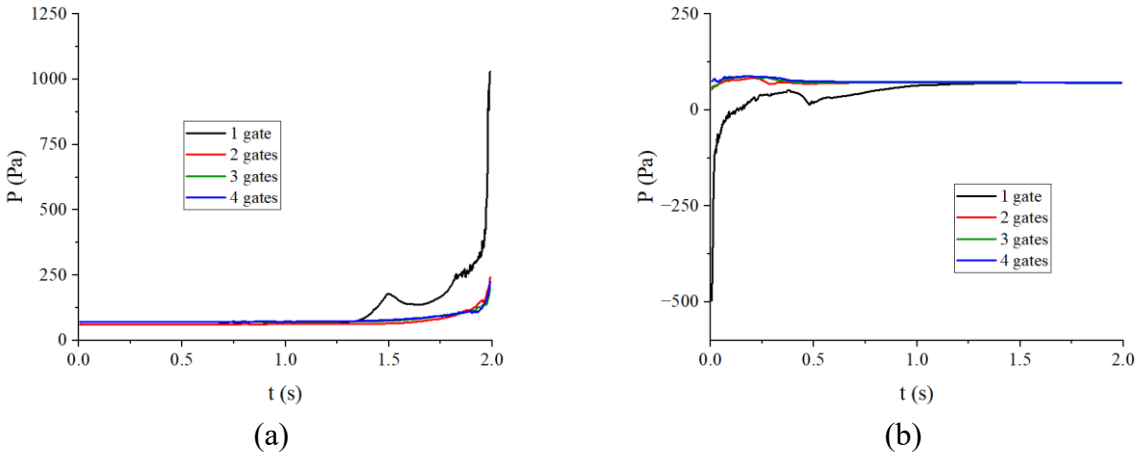

Figure 5-9- Effect of the number of gates on the pressure on the filter surface: a) gate closing, b) gate opening

5-3- Simulations with Different Gate Rotation Periods

In addition to the number of gates, the rotation speed of the gate can induce significant transient changes in the disinfection units. Thus, the objective parameters are also monitored under three gate rotation periods – shock, 2s, and 10s. A 0.25s period is considered for the shock case.

5-3-1- Effect of Rotation Period on Velocity and Acceleration

Figures 5-10a and b illustrate the evolution of the average velocity on the filter surface for the three gate movement periods for the closing and opening cases, respectively. As expected, the velocities keep dropping until they reach zero when the gates are closing. Conversely, the average velocity keeps ascending to reach 0.9 m/s when the gates open, which is sensible, as all the simulations must reach the same ultimate velocity. Thus, the initial and the final states of the simulations are similar regardless of the rotation period.

The main difference between these curves lies in the transient behavior of the velocity curves. In the gate opening case, it is seen that the velocity reaches the final value much faster than the others for the 0.25s period. However, this change is gradual and smoother for the 10s case. Thus, although the ultimate velocity values are the same, these transient changes can have substantial inertial effects on the system and particles, since the flow accelerates faster inside the disinfection unit. Thus, the acceleration values are calculated and compared as previously done for the simulations with different numbers of gates when the gates are opening.

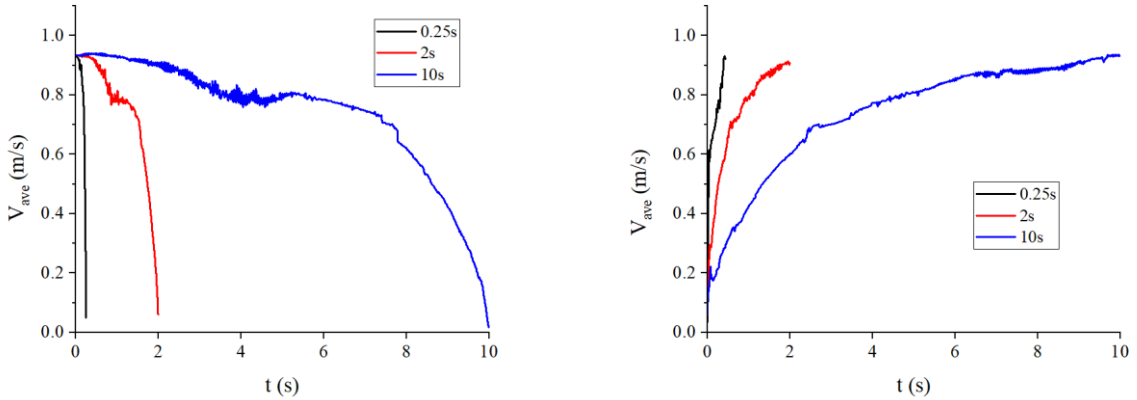

Figure 5-10- Average velocity magnitude on the filter surface: a) gate closing, b) gate opening

The acceleration vs time curves are displayed in Figure 5-11. As with previous velocity plots, these curves exhibit noticeable fluctuations, which can be due to transient flow effects and numerical noise. Among the three cases, the 0.25s case has the sharpest acceleration changes during the gate opening period, and the 10s case has smoother fluctuations. To better compare the results, the average acceleration values are compared in Figure 5-12. It is seen that the 0.25s case has an average acceleration value 11.5 times greater than the 10s case.

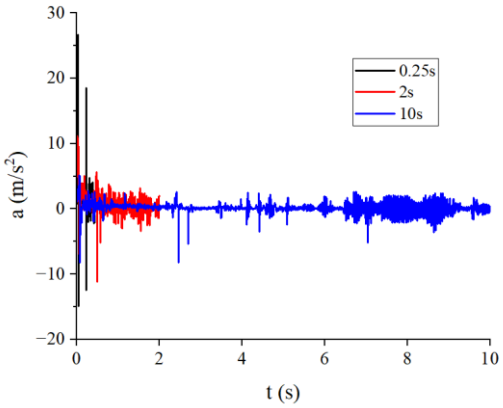

Figure 5-11- Acceleration vs time for the simulations with different numbers of gates

Thus, the 10s gate movement period performs the best among the others as it induces much less inertial and transient forces on the particles. This will result in a lower possibility of particle release from the filters.

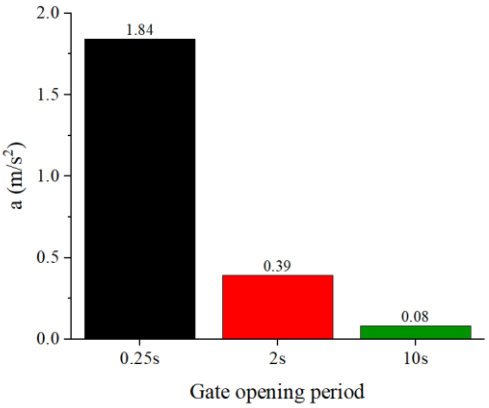

Figure 5-12- Average accelerations for different gate opening periods

5-3-2- Effect of Rotation Period on Maximum Velocity

Figures 5-13a and b illustrate the maximum velocity evolution on the filter surface over time for the gate opening and closing movements, respectively. It can be seen that when the gates are opening, the curves follow the same pattern and, in the end, they reach similar values. Moreover, the difference between the peak values is less than 4%. Thus, the gate rotation period has little impact on the maximum velocity when the gates are opening.

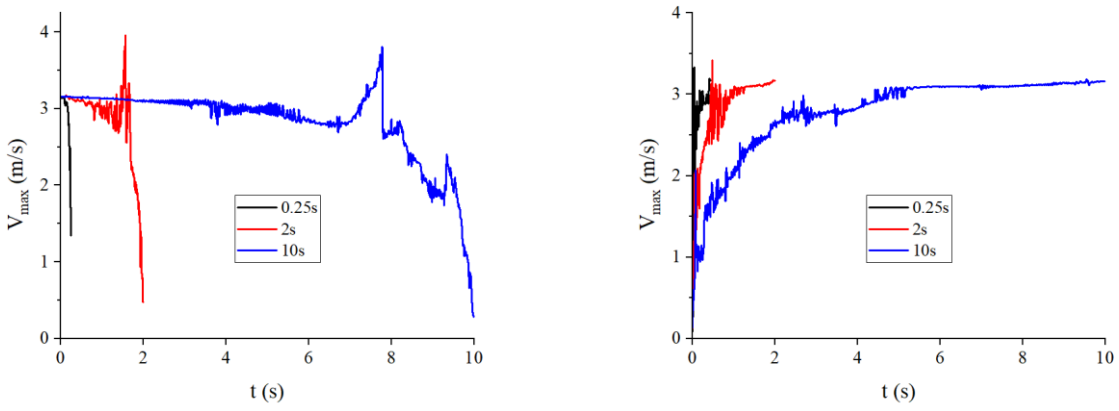

Figure 5-13- Influence of gate rotation period on the maximum velocity on the filter surface: a) gate opening, b) gate closing

In the gate closing movement, the trend is different. In contrast to the gate opening, the maximum velocity for the 2s and 10s cases peaks near the ending moments of the gate movement.

Furthermore, it is seen that the 2s and 10s cases have the same maximum velocity evolution patterns with almost the same peak values, while the maximum velocity values constantly drop for the 0.25s case. This indicates that the flow is abruptly disrupted and lacks sufficient time to form coherent velocity structures near the filter surface before the gates are fully closed.

5-3-3- Effect of Rotation Period on Turbulence

The effect of the gate rotation period on the turbulent kinetic energy on the filter surface is demonstrated in Figures 5-14a and b for the gate closing and opening cases, respectively. It can be seen that when the gates are closing, the 2s and 10s cases have a similar pattern and almost the same peak values. Thus, it can be concluded that the vortex generation and intensity are comparable for them. However, the 0.25s test demonstrates a lower TKE peak. This is due to the fast gate movement, which restricts the time required for flow structures to form and develop fully, leading to a suppressed turbulence field.

During the gate opening movement, 2s and 10s cases exhibit results similar to the gate closing scenario. However, the TKE development for the 0.25s case is quite different, and it has the highest TKE peak. The rapid opening of the gates creates sudden flow disturbance and generates high-velocity and intense vortices inside the disinfection unit.

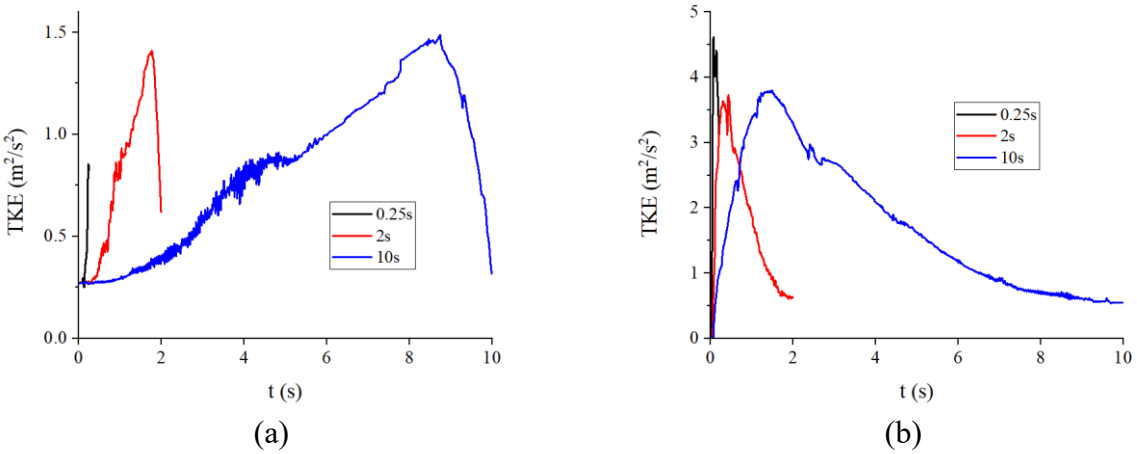

Figure 5-14- The effect of gate movement time on TKE: a) gate closing, b) gate opening

Even though the peak values do not have a remarkable difference for the 2s and 10s cases, the rate at which the turbulence grows can play a crucial role in particle release. Since turbulence induces highly fluctuating velocities on the filter surface, rapid turbulence development can impose a greater

particle release risk. To quantify this, the maximum TKE is deducted from the minimum TKE and divided by the time to reach the peak TKE value. The formulation can be found below:

$$TKE_{increase\ rate} = \frac{(TKE_{max} - TKE_{min})}{\Delta t} \tag{17}$$

The comparison is illustrated in Figure 5-15. As can be seen, the TKE increase rate reduces as the gate rotation period increases. Additionally, gate opening movement induces much higher TKE increase rates as compared to the gate closing movement.

Considering all this, it can be concluded that the 10s period results in a more controlled and gradual turbulence growth, and it is favorable.

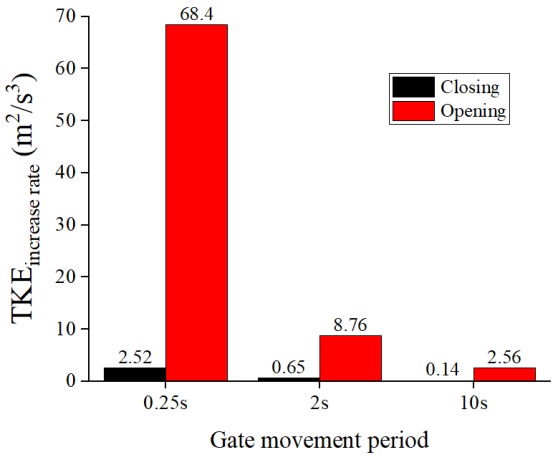

Figure 5-15- Effect of gate rotation period on TKE increase rate

5-3-4- Effect of Rotation Period on Pressure

The influence of gate rotation period on the total pressure on the filter surface is shown in Figure 5-16. In the gate closing scenario (Figure 5-16a), all three cases show a noticeable rise in pressure near the final stages of the gate movement. Although the timing of the pressure rise is different for each duration, the final peak pressures are quite similar. This suggests that gate rotation speed does not remarkably affect the pressure load on the filter during closure.

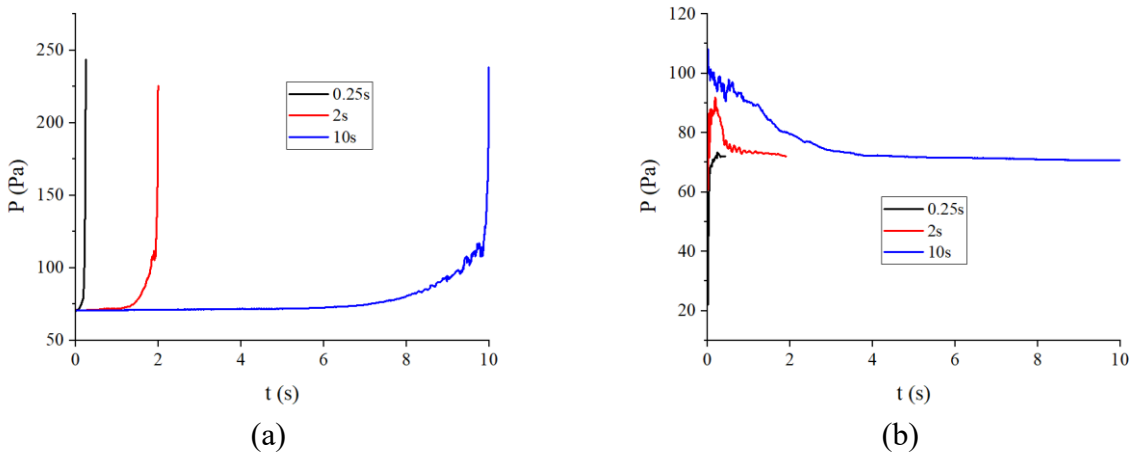

Figure 5-16- Effects of gate rotation period on the total pressure on the filter surface: a) gate closing, b) gate opening

In the gate opening movement (Figure 5-16b), it is seen that the 10s case has higher pressure at the beginning of the gate opening, which is expected because the gap between the gates stays tiny for a longer time, and it results in higher pressure values. Nonetheless, the difference is not large enough to affect the filtration capability, because, as seen in the literature review, large pressure differences in the order of a few thousand Pascals are required. Yet, the pressure difference seen in the gate opening case is in the order of a few tens of Pascals. Thus, it is concluded that the gate rotation period does not have a considerable effect on the system performance.

5-4- Particle Release Experiments

Figure 5-17 shows the particle release percentages associated with each of the gate movement speeds. It is evident that the shock case has the maximum particle release rate, and the longer gate movement period has the least amount of particle release. Moreover, the unit with the fixed open gates experiences more particle loss than the unit with moving gates. This is sensible, as the flow rate and air speed double when the gates of the other unit are closed. Since the gates were opened and closed 10 times in the experiment, the open unit experienced severe flow acceleration and velocity fluctuations.

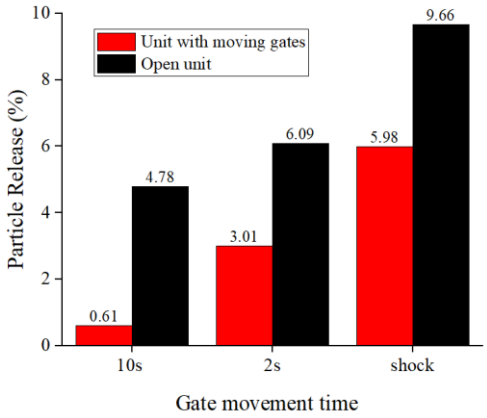

Figure 5-17- Particle release percentages for tests with different gate movement periods

5-5- Comparison of Experimental and Numerical Results

The gate rotation period experiments and numerical results provide valuable insights into the parameters affecting particle release from the filters. The experiments reveal that a longer gate movement period substantially reduces particle release. Also, it was observed in the numerical tests that as the gate rotation speed reduces, the flow acceleration reduces too. However, the maximum velocity and turbulent kinetic energy curves had almost the same maximum values for the 2s and 10s cases. The peaks of these curves were lower and higher for the 0.25s case when the gates were closing and opening, respectively. Nevertheless, the transient changes in velocity and turbulence were much sharper for the 0.25s simulation.

When comparing 2s and 10s cases in Table 5-1, it was seen that the maximum velocity and peak TKE values had negligible differences. Nonetheless, the particle release was significantly higher for the 2s case. This suggests that the transient characteristics, i.e., acceleration and TKE growth rate, were more influential.

Table 5-1- Comparison of the results for the 2s and 10s cases

Gate rotation time	Vmax (m/s)		TKE max (m^2/s^2)		TKE growth rate (m^2/s^3)		Acceleration (m/s^2)	particle release (%)
	opening	closing	opening	closing	opening	closing	opening	
2s	3.23	3.96	3.73	1.41	8.76	0.65	0.39	3.01
10s	3.18	3.81	3.81	1.49	2.56	0.14	0.08	0.61
Relative Difference (%)	-1.40	-3.94	2.01	5.38	-70.78	-78.48	-79.49	-79.73

The comparison between the 0.25s and 2s cases in Table 5-2 shows sharp changes in both TKE growth rate and acceleration. Also, maximum velocity and maximum TKE values drop when the gates open. However, these values increase when the gates are closing. Despite having lower peak velocity and TKE values when the gates are closing in the 0.25s gate closing test, the experiments show almost a 50% reduction in particle release when the gate movement period is prolonged to 2s. Thus, it can be concluded that the TKE growth rate and acceleration had the dominant effects.

It should be considered that mechanical forces were also present in the shock experiments. Since the gates were opening and closing in a fraction of a second, they were hitting the unit frame at the end of their motion, which was imposing a mechanical impact on the frame. This impact was transmitted to the filters and particles within it, too. Thus, in addition to the aerodynamic forces, the mechanical disturbances contributed to the particle release in the shock case.

Table 5-2- Comparison of the results for the 0.25 and 2s cases

Gate rotation time	Vmax (m/s)		TKE max (m^2/s^2)		TKE growth rate (m^2/s^3)		Acceleration (m/s^2)	particle release (%)
	opening	closing	opening	closing	opening	closing	opening	
0.25s	3.34	3.15	4.62	0.86	68.40	2.52	1.84	5.98
2s	3.23	3.96	3.73	1.41	8.76	0.65	0.39	3.01
Relative Difference (%)	-3.27	25.85	-19.13	64.76	-87.19	-74.31	-78.80	-49.67

These conclusions are reflected in the results of the simulations with different numbers of gates, too. Table 5-3 summarizes the results for these simulations. It is seen that the 4-gate configuration has the least amount of maximum velocity, TKE, TKE increase rate, and acceleration. Additionally, it is seen that the 1-gate configuration has a slightly lower TKE growth rate as compared to the 4-gate configuration due to its unique vortex formation nature. Yet, the peak TKE value for the 1-gate configuration is almost 5 times greater than the 4-gate configuration, and it underperforms in the other aerodynamic characteristics of the flow.

Since the reduction in the objective parameters is significant, it is inferred that the 4-gate configuration yields a more stable and less disruptive flow. Accordingly, it has the best aerodynamic conditions among the other configurations.

Table 5-3- Comparison of the results for simulations with different numbers of gates

Gate rotation time	Vmax (m/s)		TKE max (m^2/s^2)		TKE rate (m^2/s^3)		Acceleration (m/s^2)
	opening	closing	opening	closing	opening	closing	opening
1 gate	4.41	4.71	6.76	5.67	7.67	4.02	0.44
2 gates	4.67	4.34	4.18	3.23	23.14	1.82	0.39
3 gates	4.30	4.26	3.92	3.16	15.31	1.53	0.39
4 gates	3.42	3.96	3.73	1.41	8.76	0.65	0.39
Reduction for the 4-gate configuration values compared to the peak value (%)	-26.77	-15.92	-44.82	-75.13	-62.14	-83.83	-11.36

Furthermore, the 1-gate configuration has notable system design and operational setbacks in addition to having higher aerodynamic disturbances, too. Due to having the largest gate surface area among the other configurations, it will experience larger drag forces on the gate. The larger drag force will require a larger and more powerful actuator for moving the gates. Moreover, if there were a mechanical problem that hindered the gates' movement, the flow would be entirely blocked, and the system would not be operational. Thus, the 1-gate configuration is less reliable among the configurations with multiple numbers of gates.

5-6- Key Findings & Implications

The numerical tests revealed that the 4-gate configuration has the best aerodynamic response to the gate movement in both opening and closing modes. Thus, this configuration is recommended for the commercial prototype.

Additionally, the numerical and experimental tests with three gate rotation periods revealed that the longer gate rotation period is favorable. The results showed that different gate rotation periods have almost similar peak velocity and turbulence values. Yet, the transient effects and the rate of change of velocity and turbulence significantly affected particle release. Thus, gradual changes are preferred to minimize particle release risk.

Chapter 6- Conclusions & Future Work

6-1- Conclusions

The main objective of this thesis was to examine the flow behaviour as a result of the movement of the gates in the front and rear sides of the filter disinfection unit, with the aim of minimizing aerodynamic disturbances on the filter caused by the gates' movements that contribute to particle release from the filters. The key steps and findings of this thesis are listed below:

- **Wind Tunnel System Construction**
  - A wind tunnel system was designed and constructed based on ASHRAE 52.2 standard.
  - All necessary equipment was purchased, designed, and calibrated to support accurate experimental testing and numerical model validation.

- **Numerical Model Development**
  - A 2D, transient, and turbulent numerical model was developed to simulate the airflow over the gates and through the filters. The Darcy-Forchheimer model was employed to model filter media as porous media, and the filter permeability and inertial resistance were calculated using experimental measurements.
  - The numerical model was validated against the experimental data, and it was shown that the porous media modeling and the assumptions are correct, and the simplifications were reasonable.
  - This model was utilized to visualize and assess transient flow characteristics around the filters as the gates move. The dynamic mesh method was used to model the gates' movement in the computational domain.
  - Based on the literature, increasing velocity, acceleration, turbulence, and pressure were identified to enhance particle re-entrainment due to fluid flow. Thus, these parameters were selected as the main parameters to investigate in the numerical tests and were monitored on the filter surface.

- **Effects of Gate Number**
  - Simulations with units having 1, 2, 3, and 4 gates were conducted, and the effects of gate opening and closing movements were simulated for each configuration.

- The 4-gate configuration performed the best, and compared to the other configurations, it resulted in:
  - 75% lower turbulent kinetic energy (TKE)
  - 27% lower maximum velocity
  - 11% lower acceleration
- The pressure on the filter surface had similar values for the configurations with 2 to 4 gate numbers. However, the 1-gate configuration resulted in a 4 times higher pressure on the filter surface.

- **Effects of Gate Rotation**
  - Simulations with 0.25s, 2s, and 10s gate movement periods were conducted.
  - While the 2s and 10s periods had roughly the same peak TKE and velocity values, the 10s simulation resulted in 80% lower acceleration and TKE growth rate. Thus, it had much lower and smoother inertial and transient changes.
  - The 0.25s case showed the asymmetrical flow behavior during the gate opening/closing.
  - The pressure on the filter surface had similar peak values for the three gate rotation periods.
- **Particle Release Tests**
  - Experiments were designed and conducted to investigate particle release from filters during gate movement.
  - Elite clay microparticles with diameters less than 45μm were deeply embedded within the MERV 11 filters to replicate realistic filter loading conditions.
  - Particle release tests with loaded filters were done with three gate rotation periods – shock, 2s, and 10s. The gates were opened and closed 10 times with a constant rotation period for each test.
  - The results confirmed that the extreme flow agitation and transient aerodynamic changes can release particles from the filters, and sudden gate movements yielded higher particle release.
  - Gate movement with a shock results in 5.98% particle release from the filter, and 2s and 10s rotation periods yielded 3.01% and 0.61% particle release from the loaded filters.

- Mechanical impact was involved in the shock case; however, it was not measured. Yet, since the filters were subjected to mechanical impact, it can be one of the particle release intensifying factors.

In summary, the findings highlight the critical role of gate configuration and gate movement speed on the airflow disturbance and particle release from the filters. The 4-gate configuration with a 10s rotation period offered the best aerodynamic performance for minimizing particle release risk. These insights contribute to the design and operation of safer disinfection units with lower flow agitation and particle release risk, especially in spaces where air contamination control is vital.

6-2- Current Research Limitations and Future Recommendations

The current thesis is developed based on the available resources, technical equipment, and time. It was observed that in some sections, the research method can be improved to allow more in-depth analysis that requires additional equipment and resources. Recognizing these requirements, future research recommendations are listed below:

- **Recommendations related to numerical research:**
  - The gates used in the current investigation had rotational movement, and their rotation was causing remarkable flow disturbances. Other gate configurations, such as sliding gates or folding gates, can be investigated to further reduce the flow disturbance.
  - The hot-wire anemometry device used for measuring velocity did not have the capability of recording velocity over time. The accuracy of the simulations can be further increased by using a velocity meter that can record real-time transient velocities and validating numerical data against transient experimental velocity data as well.
  - Since the velocity meter could not record transient effects, turbulence intensity at the inlet and outlet boundaries could not be calculated. With a better flow velocity meter, the velocity profile can be plotted over time to calculate the inlet and outlet turbulence intensities for more accurate boundary conditions.
- **Recommendations related to experimental research:**
  - Although longer gate movement periods reduce flow agitation, they require more actuator energy to move the gates. Thus, an optimization study is recommended to find the balance between the energy consumption and flow disturbance. The actuator energy

consumption is suggested to be measured experimentally, as the gates' mass and mechanical linkage can significantly affect the energy consumption.

- This study mainly studied different gate configurations and rotation periods. However, the acceptable thresholds for velocity, acceleration, and turbulence to avoid particle release could not be determined. Advanced particle sampling methods and equipment can be utilized to determine the critical acceleration, velocity, and turbulence values for the onset of particle re-entrainment.
- Particle release from the filters was measured by calculating the weight loss of the filter after 10 times gate opening and closing movements, as the particle loss was too small for a single-cycle gate movement. However, the flow behaviors for gate opening and closing movements are different. Tools with better resolution, such as PIV laser technology or a real-time particle counter, can be utilized to study the effects of opening and closing movements separately on particle release.
- The particles were scattered on the filter surface manually. A meticulous effort was spent on the uniform dispersion and deep penetration of the particles on the filters. Yet, the filter loading method can be further refined by using a dust feeder to ensure maximum and uniform particle penetration and accumulation in the filter.
- The gates were also opened and closed by hand. When the angle of attack between the flow and the gates is large, i.e., when the gates are nearly closed or beginning to open, the drag force on the gates is large. Thus, manually opening and closing the gates at a constant speed was difficult. A controlled actuator can be designed to accurately move the gates at a constant speed.

References & Appendices

References

[1] A. Sodiq, M. A. Khan, M. Naas, and A. Amhamed, "Addressing COVID-19 contagion through the HVAC systems by reviewing indoor airborne nature of infectious microbes: Will an innovative air recirculation concept provide a practical solution?," *Environ. Res.*, vol. 199, p. 111329, Aug. 2021, doi: 10.1016/j.envres.2021.111329.

[2] L. Song *et al.*, "Airborne pathogenic microorganisms and air cleaning technology development: A review," *J. Hazard. Mater.*, vol. 424, p. 127429, Feb. 2022, doi: 10.1016/j.jhazmat.2021.127429.

[3] J. E. Yit, Y. H. Yau, and B. T. Chew, "Empirical modelling of filtration performance for the fibrous air filters with final resistance recommendation," *Results Eng.*, vol. 16, p. 100732, Dec. 2022, doi: 10.1016/j.rineng.2022.100732.

[4] Y. Xu *et al.*, "Effectiveness of heating, ventilation and air conditioning system with HEPA filter unit on indoor air quality and asthmatic children's health," *Build. Environ.*, vol. 45, no. 2, pp. 330–337, Feb. 2010, doi: 10.1016/j.buildenv.2009.06.010.

[5] C. A. Faulkner, J. E. Castellini, W. Zuo, D. M. Lorenzetti, and M. D. Sohn, "Investigation of HVAC operation strategies for office buildings during COVID-19 pandemic," *Build. Environ.*, vol. 207, p. 108519, Jan. 2022, doi: 10.1016/j.buildenv.2021.108519.

[6] "Works Cited_de38d147-30f2-44a0-ab19-676a99f2eb96.docx."

[7] E. Tian, Y. Gao, and J. Mo, "Experimental studies on electrostatic-force strengthened particulate matter filtration for built environments: Progress and perspectives," *Build. Environ.*, vol. 228, p. 109782, Jan. 2023, doi: 10.1016/j.buildenv.2022.109782.

[8] S. Mallakpour, E. Azadi, and C. M. Hussain, "Fabrication of air filters with advanced filtration performance for removal of viral aerosols and control the spread of COVID-19," *Adv. Colloid Interface Sci.*, vol. 303, p. 102653, May 2022, doi: 10.1016/j.cis.2022.102653.

[9] C. S. Heilingloh *et al.*, "Susceptibility of SARS-CoV-2 to UV irradiation," *Am. J. Infect. Control*, vol. 48, no. 10, pp. 1273–1275, Oct. 2020, doi: 10.1016/j.ajic.2020.07.031.

[10] W. J. Snelling *et al.*, "Efficacy of single pass UVC air treatment for the inactivation of coronavirus, MS2 coliphage and Staphylococcus aureus bioaerosols," *J. Aerosol Sci.*, vol. 164, p. 106003, Aug. 2022, doi: 10.1016/j.jaerosci.2022.106003.

[11] A. Skudra *et al.*, “UV inactivation of Semliki Forest virus and bacteria by alternative light sources,” *J. Photochem. Photobiol.*, vol. 10, p. 100120, Jun. 2022, doi: 10.1016/j.jpap.2022.100120.

[12] K. Guo, Y. Pan, H. F. R. Chan, K.-F. Ho, and C. Chen, “Far-UVC disinfection of airborne and surface virus in indoor environments: Laboratory experiments and numerical simulations,” *Build. Environ.*, vol. 245, p. 110900, Nov. 2023, doi: 10.1016/j.buildenv.2023.110900.

[13] M. Raeiszadeh and F. Taghipour, “Inactivation of microorganisms by newly emerged microplasma UV lamps,” *Chem. Eng. J.*, vol. 413, p. 127490, Jun. 2021, doi: 10.1016/j.cej.2020.127490.

[14] M. Alimohammadi and M. Naderi, “Effectiveness of Ozone Gas on Airborne Virus Inactivation in Enclosed Spaces: A Review Study,” *Ozone Sci. Eng.*, vol. 43, no. 1, pp. 21–31, Jan. 2021, doi: 10.1080/01919512.2020.1822149.

[15] J. Fu, Y. Xu, E. J. Arts, Z. Bai, Z. Chen, and Y. Zheng, “Viral disinfection using nonthermal plasma: A critical review and perspectives on the plasma-catalysis system,” *Chemosphere*, vol. 309, p. 136655, Dec. 2022, doi: 10.1016/j.chemosphere.2022.136655.

[16] Y. Ahmadi, N. Bhardwaj, K.-H. Kim, and S. Kumar, “Recent advances in photocatalytic removal of airborne pathogens in air,” *Sci. Total Environ.*, vol. 794, p. 148477, Nov. 2021, doi: 10.1016/j.scitotenv.2021.148477.

[17] L. Liu *et al.*, “A Review and Perspective of Environmental Disinfection Technology Based on Microwave Irradiation,” *Curr. Pollut. Rep.*, Jan. 2023, doi: 10.1007/s40726-022-00247-2.

[18] M. S. Vlaskin, “Review of air disinfection approaches and proposal for thermal inactivation of airborne viruses as a life-style and an instrument to fight pandemics,” *Appl. Therm. Eng.*, vol. 202, p. 117855, Feb. 2022, doi: 10.1016/j.applthermaleng.2021.117855.

[19] I. Bertrand *et al.*, “The impact of temperature on the inactivation of enteric viruses in food and water: a review: Virus inactivation,” *J. Appl. Microbiol.*, vol. 112, no. 6, pp. 1059–1074, Jun. 2012, doi: 10.1111/j.1365-2672.2012.05267.x.

[20] S. J. Smither, L. S. Eastaugh, J. S. Findlay, and M. S. Lever, “Experimental aerosol survival of SARS-CoV-2 in artificial saliva and tissue culture media at medium and high humidity,” *Emerg. Microbes Infect.*, vol. 9, no. 1, pp. 1415–1417, Jan. 2020, doi: 10.1080/22221751.2020.1777906.

[21] P. Dabisch *et al.*, “The influence of temperature, humidity, and simulated sunlight on the infectivity of SARS-CoV-2 in aerosols,” *Aerosol Sci. Technol.*, vol. 55, no. 2, pp. 142–153, Feb. 2021, doi: 10.1080/02786826.2020.1829536.

[22] S. A. Grinshpun *et al.*, “Inactivation of Aerosolized Viruses in Continuous Air Flow with Axial Heating,” *Aerosol Sci. Technol.*, vol. 44, no. 11, pp. 1042–1048, Sep. 2010, doi: 10.1080/02786826.2010.509119.

[23] M. Canpolat, S. Bozkurt, Ç. Şakalar, A. Y. Çoban, D. Karaçaylı, and E. Toker, “Rapid thermal inactivation of aerosolized SARS-CoV-2,” *J. Virol. Methods*, vol. 301, p. 114465, Mar. 2022, doi: 10.1016/j.jviromet.2022.114465.

[24] L. Yu *et al.*, “Catching and killing of airborne SARS-CoV-2 to control spread of COVID-19 by a heated air disinfection system,” *Mater. Today Phys.*, vol. 15, p. 100249, Dec. 2020, doi: 10.1016/j.mtphys.2020.100249.

[25] R. Zarghanishiraz, M. Zabihi, R. Li, J. Little, and V. Komisar, “Capture and thermal inactivation of airborne Covid-19 particles”.

[26] S. Zou *et al.*, “Inactivation of the novel avian influenza A (H7N9) virus under physical conditions or chemical agents treatment,” *Virol. J.*, vol. 10, no. 1, p. 289, Dec. 2013, doi: 10.1186/1743-422X-10-289.

[27] M. Hessling, N. Fehler, A.-M. Gierke, B. Sicks, and P. Vatter, “Heat Inactivation of Influenza Viruses—Analysis of Published Data and Estimations for Required Decimal Reduction Times for Different Temperatures and Media,” *Microbiol. Res.*, vol. 13, no. 4, pp. 853–871, Oct. 2022, doi: 10.3390/microbiolres13040060.

[28] R. Johne, E. Trojnar, M. Filter, and J. Hofmann, “Thermal Stability of Hepatitis E Virus as Estimated by a Cell Culture Method,” *Appl. Environ. Microbiol.*, vol. 82, no. 14, pp. 4225–4231, Jul. 2016, doi: 10.1128/AEM.00951-16.

[29] I. Leclercq, C. Batéjat, A. M. Burguière, and J. Manuguerra, “Heat inactivation of the M iddle E ast respiratory syndrome coronavirus,” *Influenza Other Respir. Viruses*, vol. 8, no. 5, pp. 585–586, Sep. 2014, doi: 10.1111/irv.12261.

[30] C. Batéjat, Q. Grassin, J.-C. Manuguerra, and I. Leclercq, “Heat inactivation of the severe acute respiratory syndrome coronavirus 2,” *J. Biosaf. Biosecurity*, vol. 3, no. 1, pp. 1–3, Jun. 2021, doi: 10.1016/j.jobb.2020.12.001.

[31] T. F. Yap, Z. Liu, R. A. Shveda, and D. J. Preston, "A predictive model of the temperature-dependent inactivation of coronaviruses," *Appl. Phys. Lett.*, vol. 117, no. 6, p. 060601, Aug. 2020, doi: 10.1063/5.0020782.

[32] J. P. Abraham, B. D. Plourde, and L. Cheng, "Using heat to kill SARS-CoV -2," *Rev. Med. Virol.*, vol. 30, no. 5, p. e2115, Sep. 2020, doi: 10.1002/rmv.2115.

[33] G. Kampf, A. Voss, and S. Scheithauer, "Inactivation of coronaviruses by heat," *J. Hosp. Infect.*, vol. 105, no. 2, pp. 348–349, Jun. 2020, doi: 10.1016/j.jhin.2020.03.025.

[34] G. Berry, I. Beckman, and H. Cho, "A comprehensive review of particle loading models of fibrous air filters," *J. Aerosol Sci.*, vol. 167, p. 106078, Jan. 2023, doi: 10.1016/j.jaerosci.2022.106078.

[35] B. Stephens, A. Novoselac, and J. Siegel, "The Effects of Filtration on Pressure Drop and Energy Consumption in Residential HVAC Systems (RP-1299)," *HVACR Res.*, vol. 16, no. 3, pp. 273–294, May 2010, doi: 10.1080/10789669.2010.10390905.

[36] G. Liu *et al.*, "A review of air filtration technologies for sustainable and healthy building ventilation," *Sustain. Cities Soc.*, vol. 32, pp. 375–396, Jul. 2017, doi: 10.1016/j.scs.2017.04.011.

[37] W. Tang, T. H. Kuehn, and M. F. Simcik, "Effects of Temperature, Humidity and Air Flow on Fungal Growth Rate on Loaded Ventilation Filters," 2015.

[38] Y. Gao, E. Tian, and J. Mo, "Electrically Responsive Coarse Filters Endowed by High-Dielectric-Constant Surface Coatings toward Efficient Removal of Ultrafine Particles and Ozone," *ACS EST Eng.*, vol. 1, no. 10, pp. 1449–1459, Oct. 2021, doi: 10.1021/acsestengg.1c00186.

[39] G. Berry, A. Parsons, M. Morgan, J. Rickert, and H. Cho, "A review of methods to reduce the probability of the airborne spread of COVID-19 in ventilation systems and enclosed spaces," *Environ. Res.*, vol. 203, p. 111765, Jan. 2022, doi: 10.1016/j.envres.2021.111765.

[40] C. Buzea, I. I. Pacheco, and K. Robbie, "Nanomaterials and nanoparticles: Sources and toxicity," *Biointerphases*, vol. 2, no. 4, pp. MR17–MR71, Dec. 2007, doi: 10.1116/1.2815690.

[41] D. Nuvolone, D. Petri, and F. Voller, "The effects of ozone on human health," *Environ. Sci. Pollut. Res.*, vol. 25, no. 9, pp. 8074–8088, Mar. 2018, doi: 10.1007/s11356-017-9239-3.

[42] A. Luengas, A. Barona, C. Hort, G. Gallastegui, V. Platel, and A. Elias, "A review of indoor air treatment technologies," *Rev. Environ. Sci. Biotechnol.*, vol. 14, no. 3, pp. 499–522, Sep. 2015, doi: 10.1007/s11157-015-9363-9.

[43] “Health Canada (2014) Residential indoor air quality guidelines, Canada.”

[44] H. Luo and L. Zhong, “Ultraviolet germicidal irradiation (UVGI) for in-duct airborne bioaerosol disinfection: Review and analysis of design factors,” *Build. Environ.*, vol. 197, p. 107852, Jun. 2021, doi: 10.1016/j.buildenv.2021.107852.

[45] F. Vranay, L. Pirsel, R. Kacik, and Z. Vranayova, “Adaptation of HVAC Systems to Reduce the Spread of COVID-19 in Buildings,” *Sustainability*, vol. 12, no. 23, p. 9992, Nov. 2020, doi: 10.3390/su12239992.

[46] Y. Xie, X. Zhu, P. Zhang, S. Wang, J. Yang, and J. Li, “Cost-effective instant air disinfection for building ventilation system by a combination of UV and micro-static electricity,” *Chem. Eng. J.*, vol. 454, p. 140231, Feb. 2023, doi: 10.1016/j.cej.2022.140231.

[47] N. Asim *et al.*, “Sustainability of Heating, Ventilation and Air-Conditioning (HVAC) Systems in Buildings—An Overview,” *Int. J. Environ. Res. Public. Health*, vol. 19, no. 2, p. 1016, Jan. 2022, doi: 10.3390/ijerph19021016.

[48] J. Wu, Y. Alipouri, H. Luo, and L. Zhong, “Ultraviolet photocatalytic oxidation technology for indoor volatile organic compound removal: A critical review with particular focus on byproduct formation and modeling,” *J. Hazard. Mater.*, vol. 421, p. 126766, Jan. 2022, doi: 10.1016/j.jhazmat.2021.126766.

[49] Y. Zhang, T. Yan, F. Wang, X. Xu, W. Jiang, and Z. Huang, “Experimental evaluation on microwave radiation disinfection efficacy of the bacterial aerosols attached to a SiC composite filter,” *Build. Environ.*, vol. 226, p. 109721, Dec. 2022, doi: 10.1016/j.buildenv.2022.109721.

[50] C. Wang, L. Song, Z. Zhang, Y. Wang, and X. Xie, “Microwave-induced release and degradation of airborne antibiotic resistance genes (ARGs) from Escherichia coli bioaerosol based on microwave absorbing material,” *J. Hazard. Mater.*, vol. 394, p. 122535, Jul. 2020, doi: 10.1016/j.jhazmat.2020.122535.

[51] Z. Liu, S. Ma, G. Cao, C. Meng, and B.-J. He, “Distribution characteristics, growth, reproduction and transmission modes and control strategies for microbial contamination in HVAC systems: A literature review,” *Energy Build.*, vol. 177, pp. 77–95, Oct. 2018, doi: 10.1016/j.enbuild.2018.07.050.

[52] J. Qian, J. Peccia, and A. R. Ferro, “Walking-induced particle resuspension in indoor environments,” *Atmos. Environ.*, vol. 89, pp. 464–481, Jun. 2014, doi: 10.1016/j.atmosenv.2014.02.035.

[53] Z. Liu, H. Niu, R. Rong, G. Cao, B.-J. He, and Q. Deng, “An experiment and numerical study of resuspension of fungal spore particles from HVAC ducts,” *Sci. Total Environ.*, vol. 708, p. 134742, Mar. 2020, doi: 10.1016/j.scitotenv.2019.134742.

[54] T. Barth, J. Preuß, G. Müller, and U. Hampel, “Single particle resuspension experiments in turbulent channel flows,” *J. Aerosol Sci.*, vol. 71, pp. 40–51, May 2014, doi: 10.1016/j.jaerosci.2014.01.006.

[55] P. Salimifard, D. Rim, C. Gomes, P. Kremer, and J. D. Freihaut, “Resuspension of biological particles from indoor surfaces: Effects of humidity and air swirl,” *Sci. Total Environ.*, vol. 583, pp. 241–247, Apr. 2017, doi: 10.1016/j.scitotenv.2017.01.058.

[56] S. Wang, B. Zhao, B. Zhou, and Z. Tan, “An experimental study on short-time particle resuspension from inner surfaces of straight ventilation ducts,” *Build. Environ.*, vol. 53, pp. 119–127, Jul. 2012, doi: 10.1016/j.buildenv.2012.01.005.

[57] S. Matsusaka, “High-Resolution Analysis of Particle Deposition and Resuspension in Turbulent Channel Flow,” *Aerosol Sci. Technol.*, vol. 49, no. 9, pp. 739–746, Sep. 2015, doi: 10.1080/02786826.2015.1066752.

[58] C. Henry, J.-P. Minier, and S. Brambilla, “Particle resuspension: Challenges and perspectives for future models,” *Phys. Rep.*, vol. 1007, pp. 1–98, Mar. 2023, doi: 10.1016/j.physrep.2022.12.005.

[59] A. H. Ibrahim, P. F. Dunn, and R. M. Brach, “Microparticle detachment from surfaces exposed to turbulent air flow: controlled experiments and modeling,” *J. Aerosol Sci.*, vol. 34, no. 6, pp. 765–782, Jun. 2003, doi: 10.1016/S0021-8502(03)00031-4.

[60] A. H. Ibrahim and P. F. Dunn, “Effects of temporal flow acceleration on the detachment of microparticles from surfaces,” *J. Aerosol Sci.*, vol. 37, no. 10, pp. 1258–1266, Oct. 2006, doi: 10.1016/j.jaerosci.2006.01.007.

[61] C. Mukai, J. A. Siegel, and A. Novoselac, “Impact of Airflow Characteristics on Particle Resuspension from Indoor Surfaces,” *Aerosol Sci. Technol.*, vol. 43, no. 10, pp. 1022–1032, Sep. 2009, doi: 10.1080/02786820903131073.

[62] F. Theron, D. Debba, and L. Le Coq, “Local experimental methodology for the study of microparticles resuspension in ventilated duct during fan acceleration,” *J. Aerosol Sci.*, vol. 140, p. 105477, Feb. 2020, doi: 10.1016/j.jaerosci.2019.105477.

[63] F. Theron, D. Debba, and L. Le Coq, “Influence of the transient airflow pattern on the temporal evolution of microparticle resuspension: Application to ventilated duct during fan

acceleration," *Aerosol Sci. Technol.*, vol. 56, no. 11, pp. 1033–1046, Nov. 2022, doi: 10.1080/02786826.2022.2120793.

[64] Z. Zhang and B. Y. H. Liu, "Experimental Study of Aerosol Filtration in the Transition Flow Regime," *Aerosol Sci. Technol.*, vol. 16, no. 4, pp. 227–235, Jan. 1992, doi: 10.1080/02786829208959551.

[65] Z. Liu, D.-R. Chen, P. Wang, and Z. Ji, "Effect of filtration pressure on the particle penetration efficiency of fibrous filter media," *Sep. Purif. Technol.*, vol. 274, p. 119086, Nov. 2021, doi: 10.1016/j.seppur.2021.119086.

[66] B. Xu, X. Yu, Y. Wu, and Z. Lin, "Experimental investigation of air pressure affecting filtration performance of fibrous filter sheet," *Environ. Technol.*, vol. 38, no. 5, pp. 558–565, Mar. 2017, doi: 10.1080/09593330.2016.1202328.

[67] D. Al Assaad, K. Ghali, N. Ghaddar, and C. Habchi, "Coupled CFD and particle resuspension models under combined effect of mechanical and aerodynamic disturbances," *Build. Environ.*, vol. 169, p. 106567, Feb. 2020, doi: 10.1016/j.buildenv.2019.106567.

[68] A. Boulbair, A. Benabed, B. Janssens, K. Limam, and W. Bosschaerts, "Numerical study of the human walking-induced fine particles resuspension," *Build. Environ.*, vol. 216, p. 109050, May 2022, doi: 10.1016/j.buildenv.2022.109050.

[69] A. Benabed, A. Boulbair, and K. Limam, "Experimental study of the human walking-induced fine and ultrafine particle resuspension in a test chamber," *Build. Environ.*, vol. 171, p. 106655, Mar. 2020, doi: 10.1016/j.buildenv.2020.106655.

[70] K. Morisseau, A. Joubert, L. Le Coq, and Y. Andres, "Quantification of the fungal fraction released from various preloaded fibrous filters during a simulated ventilation restart," *Indoor Air*, vol. 27, no. 3, pp. 529–538, May 2017, doi: 10.1111/ina.12330.

[71] E. Jankowska, T. Reponen, K. Willeke, S. A. Grinshpun, and K.-J. Choi, "COLLECTION OF FUNGAL SPORES ON AIR FILTERS AND SPORE REENTRAINMENT FROM FILTERS INTO AIR," *J. Aerosol Sci.*, vol. 31, no. 8, pp. 969–978, Aug. 2000, doi: 10.1016/S0021-8502(00)00017-3.

[72] C. Henry and J.-P. Minier, "Progress in particle resuspension from rough surfaces by turbulent flows," *Prog. Energy Combust. Sci.*, vol. 45, pp. 1–53, Dec. 2014, doi: 10.1016/j.pecs.2014.06.001.

[73] J. G. M. Kuerten, “Point-Particle DNS and LES of Particle-Laden Turbulent flow - a state-of-the-art review,” *Flow Turbul. Combust.*, vol. 97, no. 3, pp. 689–713, Oct. 2016, doi: 10.1007/s10494-016-9765-y.

[74] D. Hall, “Measurements of the mean force on a particle near a boundary in turbulent flow,” *J. Fluid Mech.*, vol. 187, pp. 451–466, Feb. 1988, doi: 10.1017/S0022112088000515.

[75] A. M. Mollinger and F. T. M. Nieuwstadt, “Measurement of the lift force on a particle fixed to the wall in the viscous sublayer of a fully developed turbulent boundary layer,” *J. Fluid Mech.*, vol. 316, pp. 285–306, Jun. 1996, doi: 10.1017/S0022112096000547.

[76] ANSYS Inc., “Defining Porous Media in Cell Zones,” ANSYS Fluent User’s Guide. Accessed: Apr. 13, 2025. [Online]. Available: https://ansyshelp.ansys.com/public/account/secured?returnurl=/Views/Secured/corp/v251/en/flu_ug/flu_ug_bcs_sec_cell_zones.html#flu_ug_sec_bc_porous_media

[77] Z. Feng, Z. Long, and Q. Chen, “Assessment of various CFD models for predicting airflow and pressure drop through pleated filter system,” *Build. Environ.*, vol. 75, pp. 132–141, May 2014, doi: 10.1016/j.buildenv.2014.01.022.

[78] W. Mrad, F. Theron, A. Joubert, N. Zgheib, and L. Le Coq, “Local variations of air velocity in the vicinity of filter pleats in transitional airflow regime – Experimental and numerical approaches,” *Sep. Purif. Technol.*, vol. 268, p. 118658, Aug. 2021, doi: 10.1016/j.seppur.2021.118658.

[79] G. Teng, G. Shi, and J. Zhu, “Influence of pleated geometry on the pressure drop of filters during dust loading process: experimental and modelling study,” *Sci. Rep.*, vol. 12, no. 1, p. 20331, Nov. 2022, doi: 10.1038/s41598-022-24838-7.

[80] L. Li *et al.*, “Research on the filtration performance of pleated filters with rectangular and triangular structures through developed CFD code,” *Prog. Nucl. Energy*, vol. 153, p. 104413, Nov. 2022, doi: 10.1016/j.pnucene.2022.104413.

[81] P. Choi, C. A. Santos, M.-K. Kim, H. Jung, D.-Y. Hong, and J. Koo, “Pressure drop and optimization meta-models for arbitrary low-height pleated filter shapes and flowrates,” *J. Mech. Sci. Technol.*, vol. 35, no. 11, pp. 5007–5022, Nov. 2021, doi: 10.1007/s12206-021-1019-9.

[82] J. Roegiers and S. Denys, “Development of a novel type activated carbon fiber filter for indoor air purification,” *Chem. Eng. J.*, vol. 417, p. 128109, Aug. 2021, doi: 10.1016/j.cej.2020.128109.

[83] Y. Alilou, S. Bourrous, T. Gélain, N. Bardin-Monnier, and D. Thomas, “Airflow characterization within the pleat channel of HEPA filters with mini pleats,” *Can. J. Chem. Eng.*, vol. 99, no. S1, Oct. 2021, doi: 10.1002/cjce.24025.

[84] A. K. Maddineni, D. Das, and R. M. Damodaran, “Numerical investigation of pressure and flow characteristics of pleated air filter system for automotive engine intake application,” *Sep. Purif. Technol.*, vol. 212, pp. 126–134, Apr. 2019, doi: 10.1016/j.seppur.2018.11.014.

[85] F. Théron, A. Joubert, and L. Le Coq, “Numerical and experimental investigations of the influence of the pleat geometry on the pressure drop and velocity field of a pleated fibrous filter,” *Sep. Purif. Technol.*, vol. 182, pp. 69–77, Jul. 2017, doi: 10.1016/j.seppur.2017.02.034.

[86] H. M. Fu, Y. Fu, and F. Xu, “Experiment and Simulation on Pressure Drop of Pleated Air Filters,” *Adv. Mater. Res.*, vol. 960–961, pp. 568–573, Jun. 2014, doi: 10.4028/www.scientific.net/AMR.960-961.568.

[87] S. Fotovati, H. V. Tafreshi, and B. Pourdeyhimi, “A macroscale model for simulating pressure drop and collection efficiency of pleated filters over time,” *Sep. Purif. Technol.*, vol. 98, pp. 344–355, Sep. 2012, doi: 10.1016/j.seppur.2012.07.009.

[88] M. Rebaï, M. Prat, M. Meireles, P. Schmitz, and R. Baclet, “A semi-analytical model for gas flow in pleated filters,” *Chem. Eng. Sci.*, vol. 65, no. 9, pp. 2835–2846, May 2010, doi: 10.1016/j.ces.2010.01.014.

[89] P. Tronville and R. Sala, “Minimization of Resistance in Pleated-Media Air Filter Designs: Empirical and CFD Approaches,” *HVACR Res.*, vol. 9, no. 1, pp. 95–106, Jan. 2003, doi: 10.1080/10789669.2003.10391058.

[90] L. Li *et al.*, “Three-dimensional numerical simulation and structural optimization of filtration performance of pleated cylindrical metal fiber filter,” *Sep. Purif. Technol.*, vol. 311, p. 123224, Apr. 2023, doi: 10.1016/j.seppur.2023.123224.

[91] S. B. Pope, *Turbulent Flows*, 1st ed. Cambridge, United Kingdom: Cambridge University Press, 2000.

[92] F. R. Menter, “Two-equation eddy-viscosity turbulence models for engineering applications,” *AIAA J.*, vol. 32, no. 8, pp. 1598–1605, Aug. 1994, doi: 10.2514/3.12149.

[93] S. Bell, “A Beginner’s Guide to Uncertainty of Measurement,” National Physical Laboratory, Teddington, Middlesex, United Kingdom, Measurement Good Practice Guide No. 11 (Issue 2), Mar. 2001.

Appendix A- Velocity Uniformity Tests

To ensure velocity uniformity, the velocity was measured at 9 points across the cross-section. (Figure 3-8 is repeated below) for two fan speeds which correspond to 802 and 2293 m3/h (472 and 1350 CFM) air flows. The sampling at each point is done 3 times, and the velocity uniformity is proved by calculating the standard deviation and coefficient of variation for each of the fan speeds. As can be seen in Tables A-1 and A-2, the coefficient of variation is 4.8% and 2.8% for 802 and 2293 m3/h air flows, respectively. Thus, it shows that the velocity is uniform across the sampling cross-section.

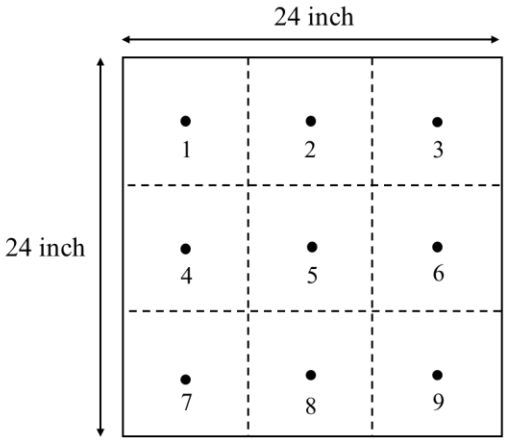

Figure 3-8- Velocity sampling points across the cross-section

Table A-1- Velocity measurements for 802 m3/h (472 CFM) air flow

Flow rate	V_P1 (m/s)	V_P2 (m/s)	V_P3 (m/s)	V_P4 (m/s)	V_P5 (m/s)	V_P6 (m/s)	V_P7 (m/s)	V_P8 (m/s)	V_P9 (m/s)
802 m3/h	0.64	0.65	0.66	0.62	0.66	0.69	0.64	0.67	0.68
	0.61	0.63	0.68	0.61	0.67	0.7	0.58	0.68	0.67
	0.58	0.7	0.68	0.64	0.65	0.73	0.6	0.65	0.68
average	0.61	0.66	0.67	0.62	0.66	0.71	0.61	0.67	0.68
mean of all points	0.65								
std.dev	0.03								
CV % (std.dev/mean)	4.84								

Table A-2- Velocity measurement for 2293 m3/h (1350 CFM) air flow

Flow rate	V_P1 (m/s)	V_P2 (m/s)	V_P3 (m/s)	V_P4 (m/s)	V_P5 (m/s)	V_P6 (m/s)	V_P7 (m/s)	V_P8 (m/s)	V_P9 (m/s)
2293 m3/h	1.7	1.69	1.76	1.74	1.73	1.79	1.77	1.77	1.79
	1.64	1.7	1.78	1.72	1.71	1.84	1.71	1.8	1.8
	1.65	1.7	1.81	1.74	1.74	1.82	1.78	1.82	1.82
average	1.66	1.70	1.78	1.73	1.73	1.82	1.75	1.80	1.80
mean of all points	1.75								
std.dev	0.05								
CV % (std.dev/mean)	2.80								

Appendix B- Pressure Transducer Calibration

The pressure transducer has two inlets, one for high pressure and the other for low pressure. Thus, the upstream flow is connected to the high-pressure end, and the downstream flow is connected to the low-pressure end. When connected, the transducer senses the pressure difference between them and sends out a voltage signal through the data acquisition system to the computer. A calibration is required to convert this voltage to pressure values.

A basic system consisting of a water column and a tube is used for the calibration (Figure B-1). The water column is placed at the same level as the pressure transducer's high-pressure end. The tube connects the bottom of the water column to the transducer's high-pressure end, and the other end is left free to contact ambient air. Then, water increments are added to the water column to increase the pressure. The resulting pressure difference is calculated using the following formula

$$\Delta P = \rho g \Delta h \tag{18}$$

In this formula, ρ is the air density, g is the gravity, and Δh is the water column height.

Figure B-1- The water column used for the pressure transducer calibration

Then, 5 pressure and voltage signals are used to calibrate the pressure transducer. These data can be seen in Table B-1.

Table B-1- Pressure drop vs transducer voltage signal

Water column height (cm)	**Pressure difference (Pa)**	**Voltage signal (V)**
0	0	1.007646
0.25	24.43	1.065004
0.5	48.85	1.200236
0.75	73.28	1.288885
1	97.70	1.433087

If the signal is in the range of each of these voltage brackets, then the voltage and pressure should be interpolated to find the pressure value. For example, if the signal is 1.04 V, the pressure value can be found by interpolating values in the first two rows as:

Voltage (V)	**Pressure difference (Pa)**
1.007646	0
1.04	? (=13.78)
1.065004	24.43

Appendix C- Particle Release Experiment Repeatability

To check the repeatability of the particle release tests, the experiment with a 2-second gate opening and closing period was repeated 3 times, and the data are reported in Table C-1. The coefficient of variance for the data related to the open unit was 3.82% and for the unit with moving gates was 13.67%.

The coefficient of variance for the unit with moving gates has a larger value as compared to the unit with open gates because the gates were opening and closing manually, and the gates' angular velocity was not confined well.

Table C-1- Data related to particle release test repeatability

Test	Filter	Particle loss %
1	F11 (open)	5.56
	F12 (moving)	2.27
2	F21 (open)	5.73
	F22 (moving)	2.29
3	F31 (open)	6.09
	F32 (moving)	3.01

For calculating the uncertainty of these experiments, the standard error of the mean can be used:

For Open unit results:

$$Mean = \bar{x} = \frac{5.56 + 5.73 + 6.09}{3} = 5.79\%$$

$$Standard\ deviation = \sqrt{\frac{(x_1 - \bar{x})^2 + (x_2 - \bar{x})^2 + (x_3 - \bar{x})^2}{n - 1}} = 0.27$$

$$Standard\ error\ of\ the\ mean = SEM = \frac{s}{\sqrt{n}} = \frac{0.27}{\sqrt{3}} = 0.16$$

In the same manner, the standard error of the mean for the tests for the unit with moving gates becomes SEM=0.24

Thus, there is $\pm 16\%$ and $\pm\ 24\%$ uncertainty errors for tests with fixed and moving gates.

Appendix D- Uncertainty of Filter Properties

Doing uncertainty analysis is an important part of every experimental study, as the uncertainty of the equipment used for measurements can accumulate and affect the experimental results. The main parameters measured in the experiments are the velocity and pressure drop, and they are used to calculate the filter permeability. Thus, the uncertainty of the permeability calculation should be calculated too.

The Darcy-Forchheimer equation (equation 7) was used to calculate the permeability and inertial resistance of the filter media. This equation is repeated below

$$\Delta P = \frac{1}{2} C_i \rho n V_{filtration}^2 + \frac{\mu n}{\alpha} V_{filtration}$$

The resultant equation, based on the pressure drop and velocity, was

$$dP = 110.01 V_{filtration}^2 + 48.015 V_{filtration}$$

If the constants of the equation above are called A and B

A=110.01 & B=48.015

Considering the Similarities with the Darcy-Forchheimer model, A and B become

$$A = \frac{1}{2} C_i \rho n$$

$$B = \frac{\mu n}{\alpha}$$

The velocity and pressure drop measuring devices have the following uncertainties

- $\delta V / V = \pm 3\%$
- $\delta \Delta P / \Delta P = \pm 0.25\%$

The uncertainties in velocity and pressure measurements contribute to the uncertainties in A and B, subsequently in α and C_i. Thus, the uncertainties of α and C_i can be calculated by calculating the uncertainties of A and B using the combined standard uncertainty [93] method.

$$\frac{\delta A}{A} = \sqrt{\left(\frac{\delta \Delta P}{\Delta P}\right)^2 + \left(2\frac{\delta V}{V}\right)^2} = \sqrt{(0.0025)^2 + (2 \times 0.03)^2} = 0.06005$$

$$\frac{\delta B}{B} = \sqrt{\left(\frac{\delta \Delta P}{\Delta P}\right)^2 + \left(\frac{\delta V}{V}\right)^2} = 0.0301$$

Accordingly, the uncertainties of inertial resistance and permeability, considering that the air and filter properties are constant, become

$$\frac{\delta C_i}{C_i} = \sqrt{\left(\frac{\delta A}{A}\right)^2 + \left(\frac{\delta \rho}{\rho}\right)^2 + \left(\frac{\delta n}{n}\right)^2} = 0.06005$$

$$\frac{\delta \alpha}{\alpha} = \sqrt{\left(\frac{\delta B}{B}\right)^2 + \left(\frac{\delta \mu}{\mu}\right)^2 + \left(\frac{\delta n}{n}\right)^2} = 0.0301$$

Thus, the uncertainty of permeability and the inertial resistance are:

$$\frac{\delta C_i}{C_i} = 6\%$$

$$\frac{\delta \alpha}{\alpha} = 3\%$$

Appendix E- User-Defined Functions

The user-defined functions listed in sections E-1 and E-2 are for gate closing movement. For the gate opening movement, the sign of the gate angular velocity, omega[2], should be changed. Additionally, the gate rotation period or time can be modified by changing the angular velocity value.

E-1- Right gate rotation (gate closing movement in 2 seconds)

```
#include "udf.h"
DEFINE_CG_MOTION(vel_udf_R,dt,vel,omega,time,dtime)
{
NV_S(vel, =, 0.0);
NV_S(omega, =, 0.0);
omega[2] = 3.1415*2;
}
```

E-2- Left gate rotation (gate closing movement in 2 seconds)

```
#include "udf.h"
DEFINE_CG_MOTION(vel_udf_L,dt,vel,omega,time,dtime)
{
NV_S(vel, =, 0.0);
NV_S(omega, =, 0.0);
omega[2] = - 3.1415*2;
}
```

E-3- Inlet velocity profile

```
#include "udf.h"
// Define the number of data points
#define N_POINTS 26
// Arrays to store y coordinates and corresponding velocities
real y_coords[N_POINTS] = {0, 0.0254, 0.0508, 0.0762, 0.1016, 0.127, 0.1524, 0.1778, 0.2032, 0.2286, 0.254, 0.2794, 0.3048, 0.3302, 0.3556, 0.381, 0.4064, 0.4318, 0.4572, 0.4826, 0.508, 0.5334, 0.5588, 0.5842, 0.5969, 0.6096};
real velocities[N_POINTS] = {0, 0.36, 0.41, 0.44, 0.45, 0.46, 0.46, 0.45, 0.45, 0.445, 0.435, 0.43, 0.42, 0.42, 0.42, 0.42, 0.425, 0.42, 0.43, 0.43, 0.43, 0.44, 0.44, 0.42, 0.375, 0};
/* Linear interpolation function */
real interpolate(real y) {
```

```
    int i;
    if (y <= y_coords[0]) {
        return velocities[0];
    }
    for (i = 1; i < N_POINTS; i++) {
        if (y < y_coords[i]) {
            real slope = (velocities[i] - velocities[i-1]) / (y_coords[i] - y_coords[i-1]);
            return velocities[i-1] + slope * (y - y_coords[i-1]);
        }
    }
    return velocities[N_POINTS-1];
}
DEFINE_PROFILE(old_filter_fan26, thread, position)
{
    real y[ND_ND]; /* This will hold the position vector */
    real y_coord;
    face_t f;
    /* Loop over all faces in the boundary */
    begin_f_loop(f, thread)
    {
        F_CENTROID(y, f, thread); /* Get the face centroid */
        y_coord = y[1]; /* Get the y-coordinate of the face centroid */
        /* Define the velocity profile using interpolation */
        F_PROFILE(f, thread, position) = interpolate(y_coord);
    }
    end_f_loop(f, thread)
}
```

Appendix F- Slurm and Journal Files Used for Cloud Computing

To carry out the simulations on the clusters, 6 files are necessary:

1- Slurm script: Used to define the time allocation and number of cores used for the simulation.
2- Journal file: Used to command Fluent to read the user-defined functions and case/data files. The number of time steps and the time step are also defined in the Journal file.
3- The case file for the simulation
4- The data file for the simulation
5- A user-defined function for the gates at the upstream of the filter
6- A user-defined function for the gates at the downstream of the filter

All of these files should be located inside a single folder in the \scratch directory of the cluster.

F-1- Slurm Script

```
#!/bin/bash
#SBATCH --account=def-anouri   # Specify account name
#SBATCH --time=2-16:00       # Specify time limit dd-hh:mm
#SBATCH --nodes=40           # Specify number of compute nodes (narval 1 node max)
#SBATCH --ntasks-per-node=10  # Specify number of cores per node (graham 32 or 44, cedar 48, beluga 40, narval 64, or less)
#SBATCH --mem=0              # Do not change (allocates all memory per compute node)
#SBATCH --cpus-per-task=1     # Do not change
#SBATCH --mail-user=erasouli@ualberta.ca
#SBATCH --mail-type=BEGIN
#SBATCH --mail-type=END
#SBATCH --mail-type=FAIL
#SBATCH --mail-type=REQUEUE
#SBATCH --mail-type=ALL
module load StdEnv/2023       # Do not change
module load ansys/2023R2      # or newer versions (beluga, cedar, graham, narval)
MYJOURNALFILE=transient.jou      # Specify your journal file name
```

```
MYVERSION=2ddp                # Specify 2d, 2ddp, 3d or 3ddp

# ------- do not change any lines below --------

if [[ "${CC_CLUSTER}" == narval ]]; then
 if [ "$EBVERSIONGENTOO" == 2020 ]; then
   module load intel/2021 intelmpi
   export INTELMPI_ROOT=$I_MPI_ROOT/mpi/latest
   export HCOLL_RCACHE=^ucs
 elif [ "$EBVERSIONGENTOO" == 2023 ]; then
   module load intel/2023 intelmpi
   export INTELMPI_ROOT=$I_MPI_ROOT
 fi
 unset I_MPI_HYDRA_BOOTSTRAP_EXEC_EXTRA_ARGS
 unset I_MPI_ROOT
fi
slurm_hl2hl.py --format ANSYS-FLUENT > /tmp/machinefile-$SLURM_JOB_ID
NCORES=$((SLURM_NNODES * SLURM_NTASKS_PER_NODE *
SLURM_CPUS_PER_TASK))
if [ "$SLURM_NNODES" == 1 ]; then
 fluent -g $MYVERSION -t $NCORES -affinity=0 -mpi=intel -pshmem -i $MYJOURNALFILE
else
 fluent -g $MYVERSION -t $NCORES -affinity=0 -mpi=intel -pib -cnf=/tmp/machinefile-
$SLURM_JOB_ID -i $MYJOURNALFILE
fi
```

F-2- Journal File Code

```
; ------------------------------------------------
; lines beginning with a semicolon are comments
```

```
define/user-defined/compiled-functions compile libudf yes 0.25s-Rotation_left-closing.c 0.25s-Rotation_right-closing.c "" ""

define/user-defined/compiled-functions load libudf

; Read the input case and data file

/file/read-case FFF.cas.h5

/file/read-data FFF.cas.h5

; Set max number of iters per time step and number of time steps

;/solve/dual-time-iterate 1000000 30 - give iterations and iterations per time step

;/solve/iterate 10000 - give iterations only for mrf

/solve/dual-time-iterate 1990 150

; Write final case and data output files

/file/write-case res

/file/write-data res

; Write simulation report to file (optional)

/report/summary y SCR_360rpm_m3.9M8BL_SBES_250129_report.txt

; Cleanly shutdown fluent

/exit
```